Design Reiteration of a Chimney Gas Flowmeter for Natural CO$_2$ Emissions from Mofettes: Differential Pressure Measurement Increases Resolution and Accuracy

A thesis submitted in fulfillment of the requirements for the degree of
Bachelor of Science in the study program of
Umweltnaturwissenschaften

University of Tübingen, Germany
at the
Center for Applied Geoscience
in the
Environmental Physics research group

Author: Kai Herrmann

First examiner: Dr. Jens Bange

Second examiner: Dr. Carsten Leven-Pfister

Supervisor: M.Sc. Yann Georg Büchau

Tübingen, 2023

Declaration of Authorship

I hereby declare that I have independently and without external assistance completed the present work. Text passages that are word-for-word or in essence based on publications or presentations by other authors are clearly identified as such. The work has not been submitted to any other examination authority and has not been published yet.

Location, Date: _____

Signed: _____

Abstract

In this thesis, an established device for in situ gas measurements of the natural CO_2 emissions from a mofetta is being improved in design and measurement principles. A cyclically erupting mofetta that is continuously submerged under the surrounding water table is observed. For the measurement of the volumetric flow rate, the previously utilized cup anemometer is discarded and instead, a self-made and self-calibrated differential pressure flowmeter is introduced. During field performance, it is validated as an accurate and high-resolution approach on flow rate quantification that is highly adapted to the conditions of the mofetta, therefore presenting a considerable improvement to the previous installment. The devices gas-channelling and sensor-carrying chimney has been redesigned completely based on a highly modular approach. This change makes field maintenance much more efficient, improving the devices flexibility by a considerable amount. Measurements on the 9th of August 2023 verified the systems ability to perform under field conditions and lead to the observation of an anomaly where the flow rate increased by ~ 40 % over the course of 1 minute coupled with a temperature rise of 0.8 K. Similarities and differences between this anomaly and anomalies detected with previous iterations of the device are discussed. High resolution pressure data is obtained which leads to a temporal quantification of the exhaust dynamics of the mofetta on a small time scale. Compared to previous measurements conduced in winter of 2022, the main frequency window in which the mofetta erupts has shifted from ~ 4 seconds to ~ 3 seconds. Furthermore, the flow rate has increased by ~ 36 - 41 % during calibration experiments and by ~ 14 - 24 % during operation. These observations suggest a seasonal dependency of the mofettas exhaust. It is discussed that this dependency may be caused by an increase in evaporation coupled with a decrease in precipitation during the summer which induces a drop in water table height. As a consequence, the hydrostatic pressure the upstreaming gas needs to overcome to reach the atmosphere decreases, resulting in a rise in frequency and consequentially an increase in flow rate.

Contents

1 Introduction

The correlation between continuous rising carbon dioxide (CO_2) concentrations in the earth's atmosphere and global warming is well documented and undenied within the scientific community (Cook et al., 2016). The complexity of the climate system and the uncertainty of how the introduction of greenhouse gasses like CO_2 affect earth's ecosystems on a large temporal scale catch the attention of researchers, politicians and the general public more than ever (Anderson et al., 2016). Besides anthropogenic sources, there are many types of natural CO_2 emissions ranging from active geothermal systems in deep ocean (Marty & Tolstikhin, 1998), mofettes (Lübben & Leven, 2018), organic carbon release in soils (Sarzhanov et al., 2017) to volcano outbursts (Martini, 1997). Monitoring and quantifying these emissions is highly relevant in order to asses their impact on the atmosphere's carbon budget and to discover possible links processes that mitigate or amplify these emissions (Camarda et al., 2019).

The Environmental Physics research group of the University of Tübingen has established an autarkic monitoring sensor network in the upper Neckar valley as part of the CO_2 Monitoring Project (Büchau et al., 2022). Its objective is to quantify natural CO_2 emissions of geologic origin. Besides diffuse degassing, the measuring site is characterized by localized degassing of CO_2, so called mofettes. Multiple sensor stations aim to quantify different aspects of these emissions, all of which are embedded into a wireless network infrastructure and are largely low-cost. Based on principles similar to the ones used by Schütze et al. (2015), Hörmle (2019) developed a monitoring device for estimating the emissions of such a mofetta. This instrument established a two-part design with a halved plastic bucket that is placed on top of the mofetta and a sensor-carrying chimney through which the gas is directed outwards (Hörmle, 2019). Later titled **mo**fetta**ho**od, or **MoHo** for short, Mühlberger (2020) and Dörner (2022) have continuously improved this device under the supervision of Yann Büchau, resulting in the latest **v**ersion 3.2 (**v**3.2). The main goal of all MoHo reiterations is to improve the device's capability to reliably detect and quantify trends and anomalies in the mofetta's exhaust. The investigated mofetta has stayed the same since Mühlberger (2020), a mofetta constantly submerged under the water table of the wetland area. Latest measurements by Büchau et al. (2023) have lead to the quantification of the dynamics in its degassing.

This work further improves the MoHo v3.2 in both design and measurement principles. The focus lies on the volumetric flow rate measurement principle, which has been reiterated through the introduction of a differential pressure flowmeter. The design, calibration and field performance of this flowmeter is presented and discussed.

Additional focus is placed on the functionality and design of the sensor-carrying chimney which has been completely overhauled over the course of the flowmeter implementation. The finalized setup has been deployed in the field on the 9th of August 2023, the measurements of which are displayed and discussed. Findings will be contextualized through the comparison with previous measurements conducted by Büchau et al. (2023) with the MoHo v3.2 in February of 2022. The implications of differences that emerge through this comparison will be discussed in the final section of the thesis.

2 Measuring Site & Previous Mofetta Hood Version

2.1 Measuring Site

The measuring site is located in Baden-Württemberg in the southwestern part of Germany within the upper Neckar valley (Figure 1 a). In the municipality of Starzach, shortly south of the name giving Neckar river, a meadow spanning about two hectares is characterized by natural degassing of CO_2 (Büchau et al., 2022). The location of interest is confined by the northern and southern slopes of the valley (Figure 1 b). Due to its characteristics, this region was used for industrial gas mining since 1895 until CO_2 yields declined, resulting in a stop in 1995 (Lübben & Leven, 2018).

With the Alpine orogeny, the formation of large tectonic structures took place and parts of the lithosphere were uplifted, deformed and thinned. This lead to the activation of accessible subsurface structures, serving as preferential fluid pathways. Lithospheric mantle material experienced a decrease in pressure, causing its mobilization and upward movement. This led to regions of basaltic volcanism during the Tertiary age, for example in the Bad Urach volcanic region. Apart from the Alps and Upper Rhine Graben, this region is not affected by recent tectonic activities (Lübben & Leven, 2018).

The most recent explanation for the natural CO_2 exhalations at the site was proposed by Lübben & Leven (2018). Based on its chemical composition, the gas likely originates from the earth's upper mantle. Due to the cooling of magma, slightly soluble volatiles, such as carbon dioxide, degas and migrate upwards. It is assumed that the sandstone deposits of the Middle and Lower Buntsandstein act as a reservoirs for the accumulation of ascending CO_2. The upper located silt- and clay-heavy Röt formation caps the upstreaming gas due to its low porosity. At the Starzach site, a fault zone is assumed to penetrate the clay of the Röt formation, creating cracks through which CO_2 can stream upwards. From there, the gas leaks into the

stratigraphic layer of the Lower Muschelkalk, where it makes its way into the lower atmosphere (Lübben & Leven, 2018).
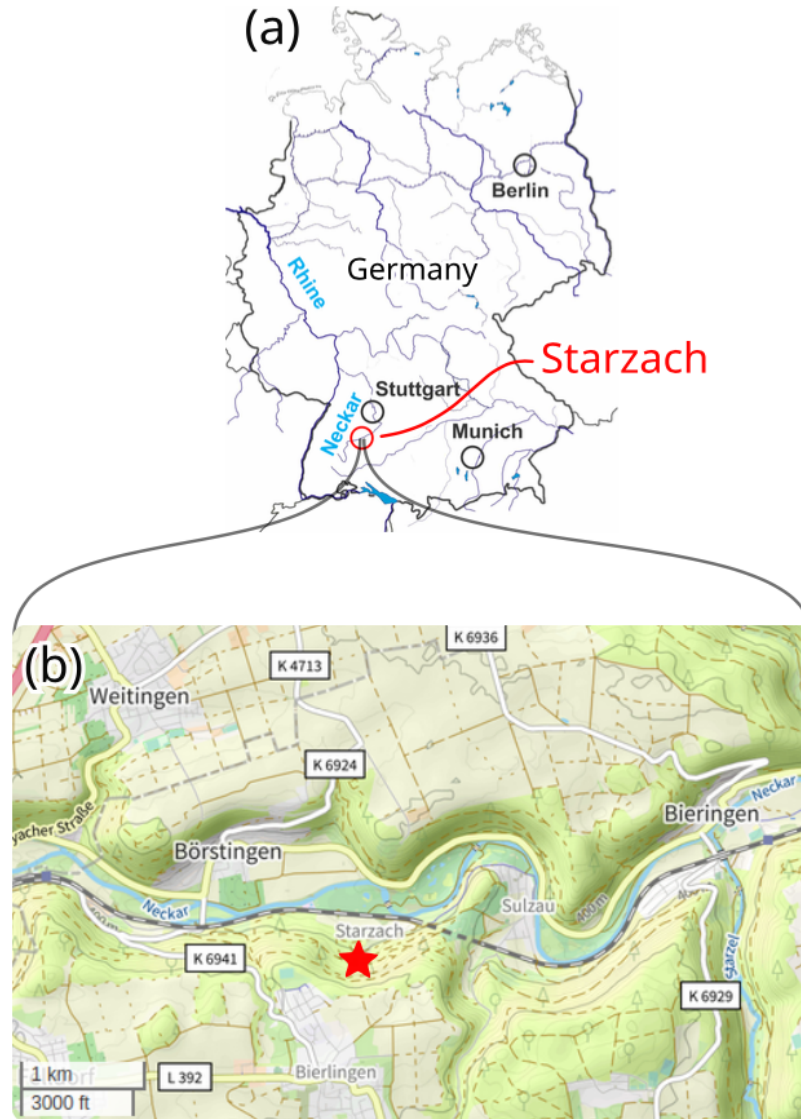

Figure 1: (a) Geographic location of Starzach (b) Map of Neckar Valley with location of measuring site marked by a star (Büchau et al., 2023, licensed under the CC BY Attribution 4.0 International licence). The original, unadapted version of (b) is by OpenStreetMap contributors, 2023 that is licensed under the Open Database License. The map used in (b) is by Tracestrack.

The meadow features numerous locally concentrated areas of strong, natural advective CO_2 exhalation called mofettes (singular: mofetta) (Figure 2). Technically, the exhaled gas is a gas mixture that also features small amounts of oxygen, methane, nitrogen and noble gases, with CO_2 making up the largest amount (Lübben & Leven, 2018). Most mofettes are submerged continuously under the water table surfacing in the area, called "wet mofettes", in contrast to the ones directly exposed to the atmosphere, called "dry mofettes" (Büchau et al., 2022).

Figure 2: Wet (blue dot) and dry (red dot) mofettes at the Starzach measuring site. The wet mofetta that is being investigated in this thesis is marked by a blue star. The drone picture was taken by Martin Schön in summer of 2019. The mapping is adapted from Büchau et al. (2022).

2.2 Investigated Mofetta

The investigated mofetta is a wet mofetta located at the southern end of the meadow (Figure 2). In May of 2014, a 5.08 cm groundwater monitoring well (DN50) was installed at this very location that reaches a depth of up to 9.4 meters (Figure 3, Figure 4). At the time of installation, the well did not show any significant gas exhalation. However, until the end of that year, a mofetta formed, likely as a consequence of the favorable pathway presented by the well. Its exhalation increased over the years, making it nowadays the mofetta with the currently strongest gas outflow at the site (Büchau et al., 2023).
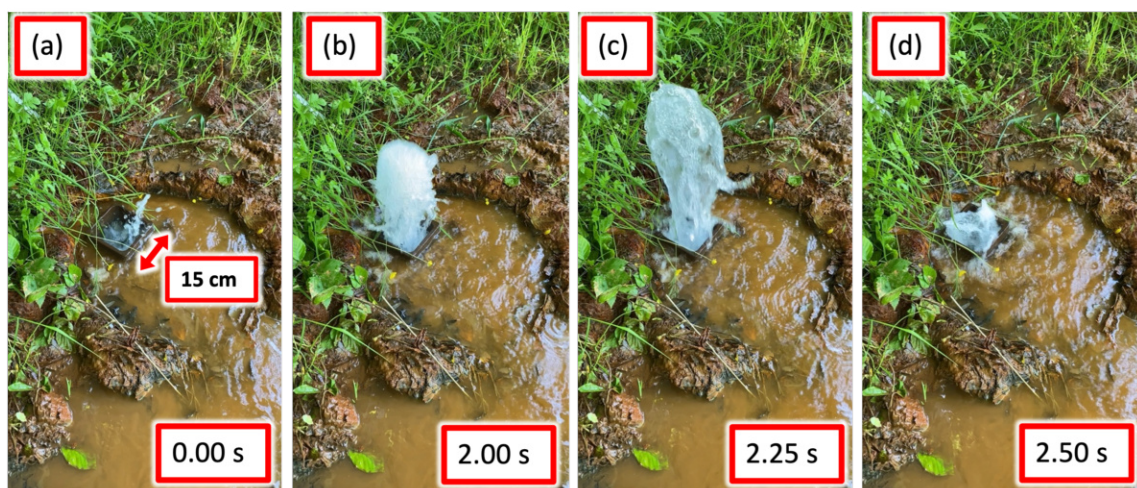

Figure 3: Cyclic eruptions characterizing the investigated mofetta divided into bubble (a), burst (b, c) and collapse state (d). Taken on the 2nd of June 2023. Time stamps in seconds since beginning of bubble state.
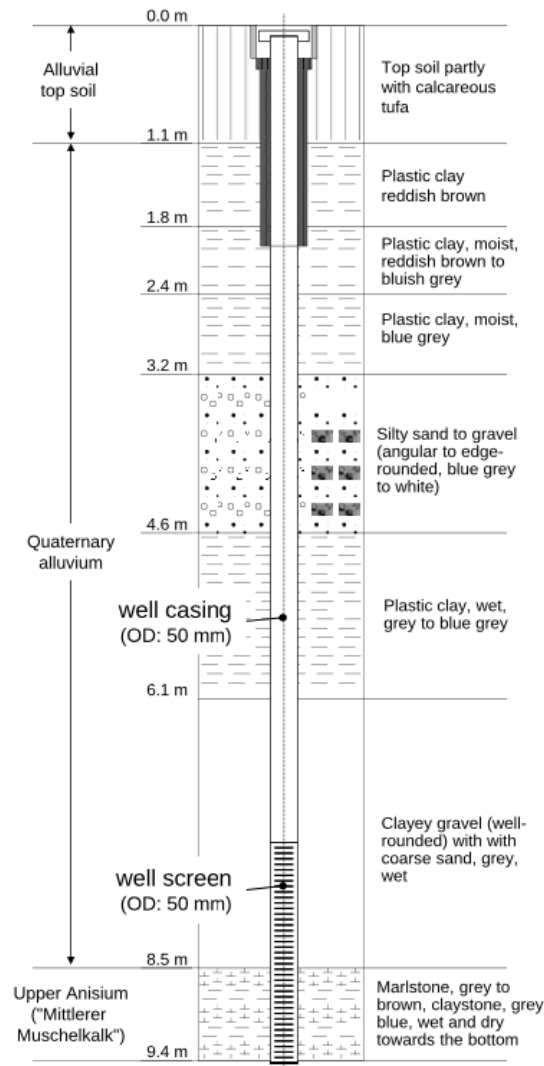
Figure 4: Borehole log around groundwater monitoring well at location of investigated mofetta with lithological classification (Büchau et al., 2023, licensed under the CC BY Attribution 4.0 International licence).

Wet mofettes are characterized by degassing through bubbling. In the case of the investigated mofetta, small eruptions happen cyclically (Figure 3). This is caused by a periodic shift of pressure equilibrium within the groundwater monitoring well. The gas rises up through favorable pathways and enters the well through the perforations of the well screen (Figure 4). At this depth, the gas needs to overcome the hydrostatic pressure of the water column within the well of more than 60 kPa. To overcome this counteracting force, enough gas needs to accumulate first (Figure 3 a) in order to built-up pressure that eventually exceeds the hydrostatic pressure and results in rapid gas release in the form of an eruption (Figure 3 b, c) (Büchau et al., 2023). During operation of the MoHo v3.2 in February of 2022, this cycle has been quantified by Büchau et al. (2023) with 3 - 5 seconds being responsible for more than half of the total signal variance of the volumetric flow rate signal ("4-s-cycle"). Furthermore,

Büchau et al. ([2023](#)) captured an anomaly twice within the span of 60 hours where the volumetric flow rate increased rapidly by $\sim 25\,\%$ within a few minutes before gradually falling back to the previous level within the next ~ 24 hours.

2.3 Previous Version of the Mofetta Hood

To determine the CO_2 mass flux ([subsection 3.1](#)) of the mofetta, Büchau et al. ([2023](#)) utilized chimney segments made out of **g**lycol-modified **p**oly**e**thylene **t**erephthalate (**PETG**) that are placed into one another by a thread mechanism ([Figure 5](#) a).
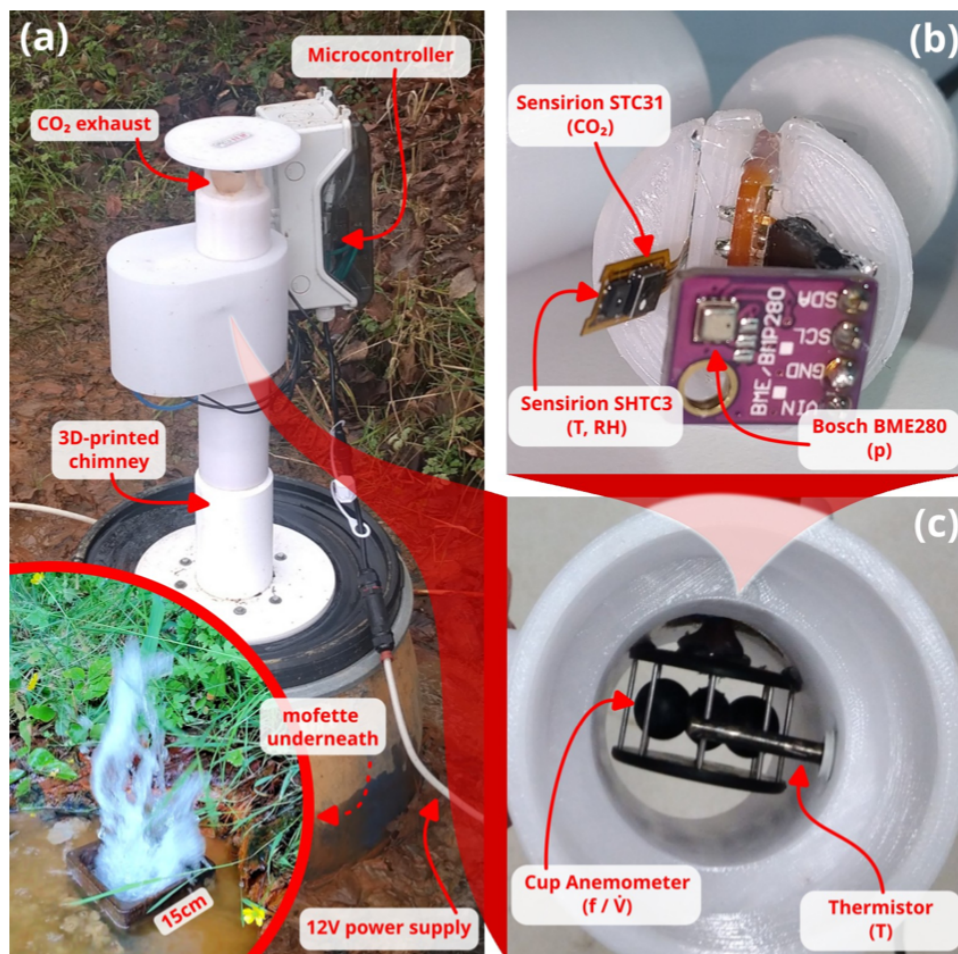
Figure 5: (a) MoHo v3.2 on top of the mofetta in February of 2022 (b) Sensor cave housing the Sensirion STC31 & SHTC3 and Bosch BME280 (c) View through the chimney from below (Büchau et al., [2023](#), licensed under the [CC BY Attribution 4.0 International](#) licence).

For volumetric CO_2 concentration measurements, the **s**ensor **e**valuation **k**it (**SEK**) of the Sensirion STC31 CO_2 sensor in combination with the Bosch BME280 pressure sensor was selected. The SEK-STC31 consists of a flexible printed circuit, on the tip of which the Sensirion STC31 and SHTC3 are affixed ([Figure 5](#) b). All three sensors accessed the gas indirectly by being vertically inserted into the chimney in

the form of a sensor cave (Figure 5 b, c) (Dörner, 2022; Büchau et al., 2023). In the same segment, a thermistor was directly inserted into the chimney cavity to deliver temperature values (Figure 5 c). The thermistor helped to identify and validate the flow rate anomalies captured by Büchau et al. (2023). A significant temperature drop corresponding with these anomalies was detected that was likely attributed to the suction of outside air into the chimney (Büchau et al., 2023). Since both the thermistor and Sensirion SEK-STC31 are kept in the new MoHo version, their working principle will be explained in detail in subsection 3.4.

For measuring the volumetric flow rate, the MoHo v3.2 incorporated a cup anemometer that was taken out of a handheld device (Figure 5 c). The rotational frequency of the cups was detected through a hall-sensor coupled with magnets installed close to the rotational axis and then converted into a volumetric flow rate through calibration against the LTG 227VM-05 volumetric flow sensor (Büchau et al., 2023). During operation, this approach revealed inefficiencies like the mechanical susceptibility of the moving cups, unreliable data output of the hall-sensor as well as difficult reproducibility due to the lack of commercially available small-sized cup anemometers. This is why in this thesis, an alternative volumetric flow rate measurement technique is developed for the new MoHo version that addresses these issues.

As a proof of concept for the flow rate calibration, Büchau et al. (2023) used trash bags of differing sizes and placed them on top of the chimney during operation ("bag experiments"). Through measuring the time it takes for a trash bag to be filled completely by the gas and estimating the total volume, mean volumetric flow rates were derived. By comparing these values to the corresponding volumetric flow rates measured by the anemometer, Büchau et al. (2023) assessed weather the calibration is correct and applicable under field conditions. This concept will be expanded upon for the calibration of the differential pressure flowmeter (subsubsection 3.5.2).

3 Methods

3.1 CO_2 Mass Flux Calculation

For the derivation of the CO_2 mass flux $\dot{m}_{CO_2}$ through the chimney, an ideal gas is assumed, providing the perfect gas law as the foundation for the calculation with

$$p \cdot V = n \cdot R^* \cdot T \tag{1}$$

and

p = Pressure [Pa]
V = Volume [m^3]
n = Amount of substance [mol]
R^* = Gas constant ≈ 8.314 J mol^{-1} K^{-1}

as well as the temperature T in Kelvin (Atkins & Paula, 2006). Through the introduction the molar mass $M_{CO_2} \approx 0.044$ kg mol^{-1} of CO_2 and the volumetric CO_2 concentration X_{CO_2} [parts per million] in Equation 1, an expression for the mass m_{CO_2} [kg] with

$$m_{CO_2} = X_{CO_2} \cdot \frac{p \cdot V}{R_s \cdot T} \tag{2}$$

and $R_s = \frac{R^*}{M_{CO_2}} \approx 188.92$ J kg^{-1}K^{-1} is obtained. The partial derivative of Equation 2 with respect to the time t leads to an expression for the temporal change in m_{CO_2} [kg s^{-1}]:

$$\partial_t\, m_{CO_2} = \dot{m}_{CO_2} = X_{CO_2} \cdot \dot{V} \cdot \frac{p \cdot M_{CO_2}}{R^* \cdot T} \tag{3}$$

In Equation 3, the volumetric CO_2 concentration X_{CO_2}, pressure p and temperature T were assumed to be constant in time. This assumption simplifies the calculation of the mass flow rate significantly and is reasonable for high sampling rates of the volumetric flow rate $\dot{V}$ (~ 100 Hz).

3.2 Chimney Design

The main two-part design of the MoHo stays the same for the new **v**ersion 4.0 (**v**4.0) (Figure 6). However, the chimney has been redesigned completely in order to improve the modularity of the measuring setup. All of the parts have been 3D-printed using **p**oly**l**actic **a**cid (**PLA**) filaments and designed using a fork created by Büchau (2023b) based on a python package by Fogleman (2022). A highly modular approach on design makes the individual sensors more accessible and therefore their exchange in case of malfunction more efficient, improving the MoHo's flexibility.
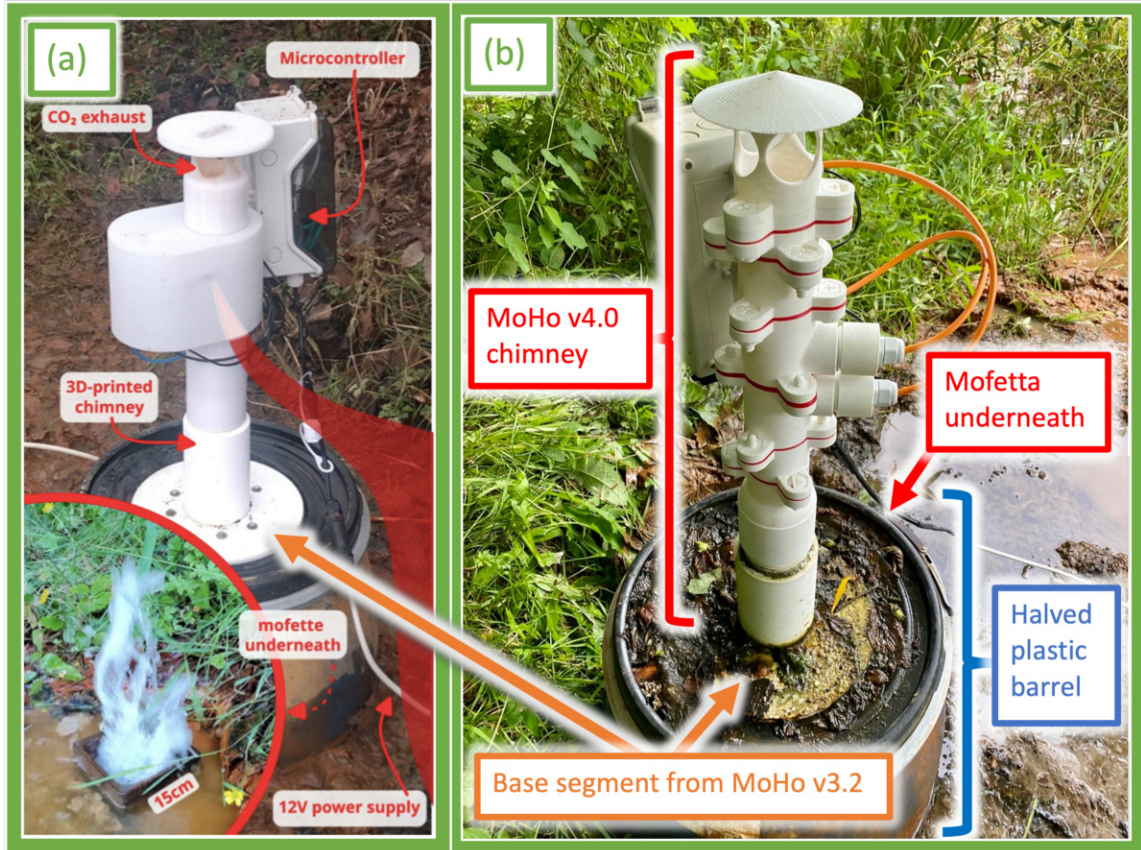
Figure 6: (a) MoHo v3.2 on top of the mofetta in February of 2022 (adapted from Büchau et al., 2023, licensed under the CC BY Attribution 4.0 International licence) (b) MoHo v4.0 with gas-channelling barrel and overhauled sensor-carrying chimney on top of the mofetta on the 9th of August 2023.

The functionality of each segment is decreased so that one segment only fulfills one function (Figure 7). The previous threaded connection mechanism (Figure 6 a) is discarded. Instead, triplets of flanges are installed at both ends of a segment, allowing for a connection through screws and nuts (Figure 7). Flexible, red-coloured sealing rings that were 3D-printed using **t**hermoplastic **p**oly**u**rethane (**TPU**) filaments are clamped in between the segments to minimize leakage of upstreaming gas (Figure 7). The base segment already mounted onto the plastic bucket (Figure 6 a) remains the same (Figure 6 b). Therefore a transition segment, that translates the from the previous to the new connection design is installed (Figure 7 a). The thermistor from the previous design is kept and positioned in the center of the chimney by being vertically inserted through a cable gland (Figure 7 b, Figure 8 a).
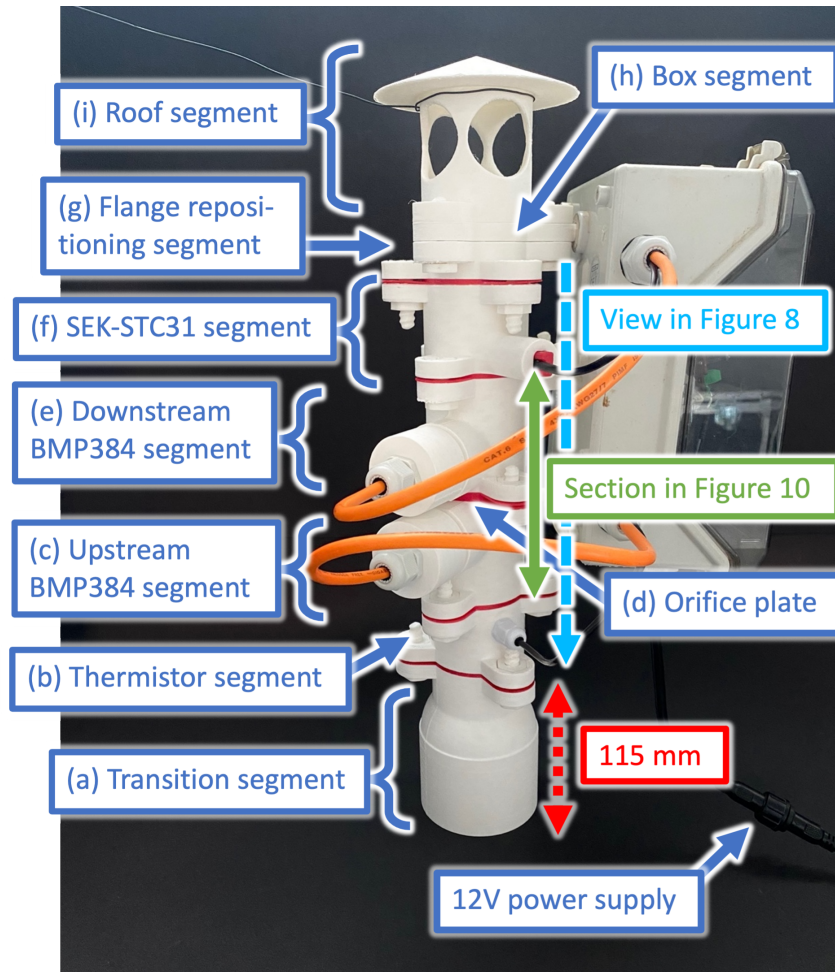
Figure 7: Segment-based chimney for the MoHo v4.0 with the electrical enclosure box attached onto the box segment. All segments except the bottom, widened part of the transition segment show an inner diameter of $D = 55$ mm.
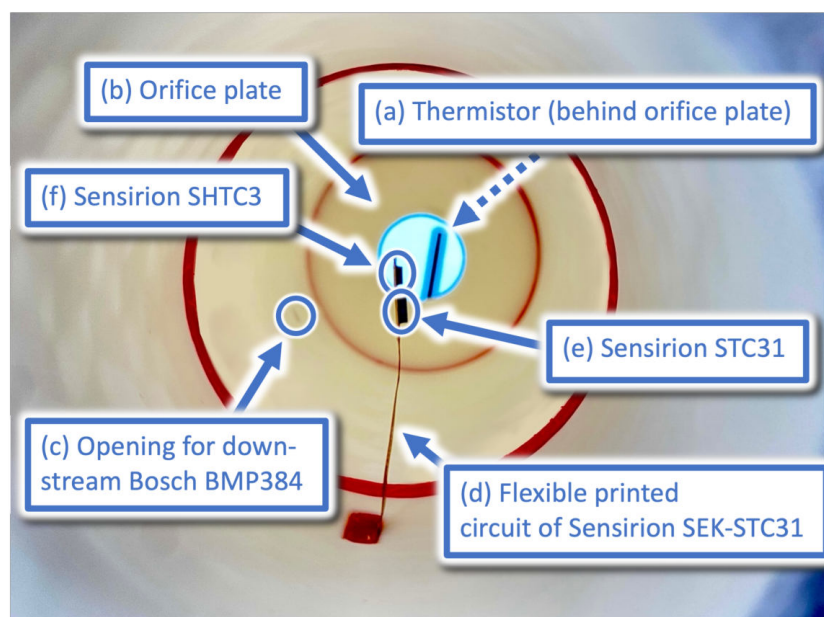
Figure 8: View through chimney as marked in Figure 7.

As part of a differential pressure flowmeter, pressure sensor segments are installed up- and downstream of an orifice plate (Figure 7 c - e). The segments implement a hollow, threaded protrusion on the outside wall for the placement of the BMP384 SparkFun pressure sensor (Figure 9 a). This sensor consists of a 25.4 mm by 25.4 mm printed circuit board at the center of which the name giving 2 mm x 2 mm Bosch BMP384 pressure sensor is installed (Figure 9 b, c). A hollow screw cap clamps the board into place (Figure 9 f) so that the Bosch BMP384 pressure sensor has access to the chimney through a size- and position-matching hole (Figure 8 c, Figure 10 a). The orifice plate is a 3 mm thick plate with a concentric circular opening of the diameter d through which the upstreaming gas is forced through (Figure 10 b, c).

Figure 9: Parts of the downstream BMP384 segment as seen in Figure 7 e.

Figure 10: Halved sections of differential pressure flowmeter seen in Figure 7 c - e

Compared to the previous sensor-cave-based design (Figure 5 b, c), the Sensirion SEK-STC31 is inserted directly into the chimney through a hollow protrusion on the outside wall and held in place by a screw mechanism (Figure 7 f). The flexible printed circuit is positioned in such a way, so that the STC31 and SHTC3 are located at the center of the chimney (Figure 8 d - f). By accessing the upstreaming gas directly, more 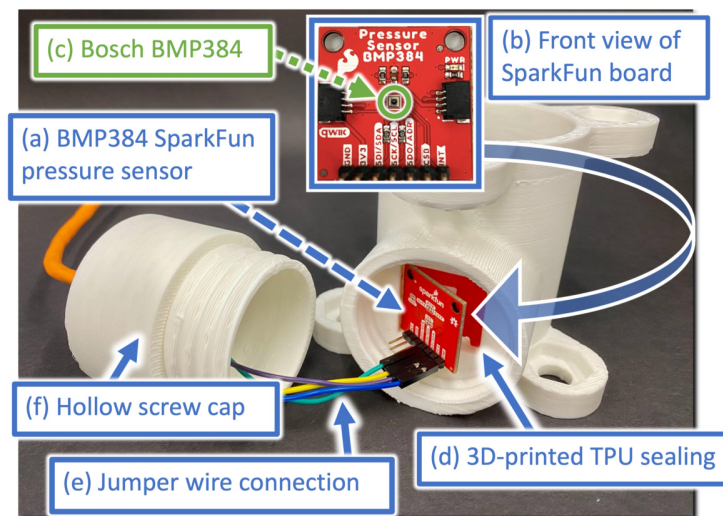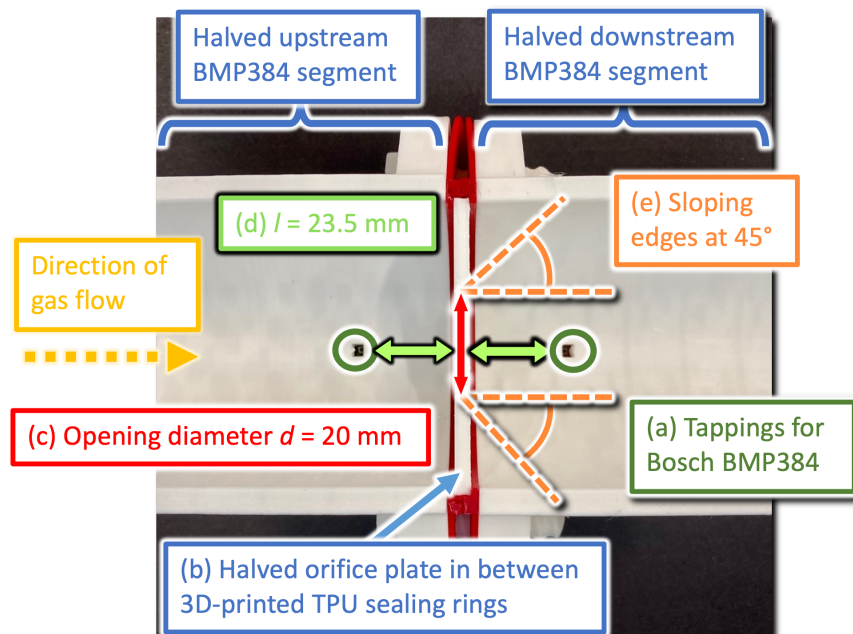representative volumetric CO_2 concentration data is retrieved. To minimize the risk of malfunction due to water vapor condensation, the CO_2 sensor segment is positioned close to the upper end of the chimney (Figure 7 f).

A segment with a vertical screw allows for the attachment of a Hensel KG 9001 electrical enclosure box (Figure 7 h). For all of the segments, upper and bottom flange triplets are displaced by an angle of 60° relative to each other (Figure 7). To achieve the desired position for the electrical enclosure box, a segment translating between the angles, is used (Figure 7 g). A roof segment minimizes the fall of rainwater and debris into the chimney whilst allowing the upstreaming gas to leaf the MoHo (Figure 7 i).

3.3 Differential Pressure Flowmeter

A common way to measure the volumetric flow rate of a fluid is through a differential pressure flowmeter. A constriction is integrated into a tube with an inner diameter D through which the fluid is passed through. A widely spread type of constriction in differential pressure flowmeters is an orifice plate, a thin plate with a concentric circular opening (Figure 8 b, Figure 10 b, c) that reduces the cross-sectional area of the flow path (Bentley, 2005). An orifice plate is the most suitable construction to implement into the MoHo chimney due to its cost-effectiveness and since it can be altered and swapped easily depending on measurement results during calibration.

As the fluid passes through the orifice plate, its velocity v increases and pressure P drops. This relationship is described by Bernoulli's principle (Bentley, 2005) with

$$P + \frac{1}{2} \cdot \rho \cdot v^2 + \rho \cdot g \cdot h = \text{constant} \qquad (4)$$

and
$P =$ Fluid or static pressure [Pa]
$\rho =$ Fluid density [kg m^{-3}]
$v =$ Velocity of the fluid [m s^{-1}]
$g =$ Gravitational acceleration [m s^{-2}]
$h =$ Elevation [m]

Along a given streamline, the sum of the static, dynamic and hydrostatic pressure remains constant (Equation 4). For Bernoulli's principle to be applicable, the fluid needs to show a local stationary velocity field, needs to be inviscid, meaning shear forces due to viscosity are negligible, and incompressible, meaning the density ρ remains constant throughout the flow (Bentley, 2005). When comparing the flow at an up- and downstream location along a streamline, Bernoulli's principle states that:

$$P_{\text{upstream}} + \frac{1}{2} \cdot \rho \cdot v_{\text{upstream}}^2 + \rho \cdot g \cdot h_{\text{upstream}} = P_{\text{downstream}} + \frac{1}{2} \cdot \rho \cdot v_{\text{downstream}}^2 + \rho \cdot g \cdot h_{\text{downstream}} \tag{5}$$

For horizontal flow, the hydrostatic pressure terms cancel out since $h_{\text{upstream}} = h_{\text{downstream}}$. The change in pressure ΔP across the constriction is expressed by:

$$\Delta P = P_{\text{upstream}} - P_{\text{downstream}} = \frac{1}{2} \cdot \rho \cdot (v_{\text{downstream}}^2 - v_{\text{upstream}}^2) \tag{6}$$

The cross-sectional area of the fluid shortly before the orifice plate on the upstream side (A_{upstream}) and on the downstream side ($A_{\text{downstream}}$) changes with the flow rate and can therefore not be measured accurately. Due to the converging of streamlines, $A_{\text{downstream}}$ is smaller than the area $A_d = \frac{\pi \cdot d^2}{4}$ enclosed by the orifice plate's opening of the diameter d. A_{upstream} can only be assumed to be equal to $\frac{\pi \cdot D^2}{4}$ if the fluid fills up the pipe completely (Bentley, 2005). In order for the mass m of the incompressible fluid to be preserved, the mass flow rates $\dot{m}_{\text{upstream}}$ and $\dot{m}_{\text{downstream}}$ must be equal:

$$\dot{m}_{\text{upstream}} = \dot{m}_{\text{downstream}} \tag{7}$$

$$\rho \cdot A_{\text{upstream}} \cdot v_{\text{upstream}} = \rho \cdot A_{\text{downstream}} \cdot v_{\text{downstream}} \tag{8}$$

Since the cross-sectional area A_{upstream} is bigger than $A_{\text{downstream}}$, the ratio $\frac{A_{\text{upstream}}}{A_{\text{downstream}}}$ is bigger than one. Therefore $v_{\text{downstream}}$ is greater than v_{upstream}. Through combining Equation 6 and Equation 8, the change in pressure can be expressed as:

$$\Delta P = \frac{1}{2} \cdot \rho \cdot v_{\text{upstream}}^2 \cdot \left(\frac{A_{\text{upstream}}^2}{A_{\text{downstream}}^2} - 1 \right) \tag{9}$$

ΔP is bigger than zero since $v_{\text{downstream}} > v_{\text{upstream}}$, meaning the pressure drops along the constriction. Because of frictional effects, a permanent decrease in pressure is developed downstream of the orifice plate (Bentley, 2005).

Usually, in differential pressure flowmeters, the volumetric flow rate $\dot{V}$ of the fluid is obtained by determining the differential pressure developed across the orifice plate through measuring the local pressure at the tube's edges. For this, pressure measured at the edges of the tube is assumed to be the same as pressure in the fluid along the

planes of A_{upstream} and $A_{\text{downstream}}$ due to the presence of recirculation zones (Bentley, 2005). By building upon the following parametrization

$$\dot{V} = \dot{V}_{\text{upstream}} = v_{\text{upstream}} \cdot A_{\text{upstream}} \tag{10}$$

a theoretical equation for incompressible fluid flow $\dot{V}_{\text{theoretical}}$ can be obtained with

$$\dot{V}_{\text{theoretical}} = A_{\text{upstream}} \cdot \sqrt{\frac{2 \cdot \Delta P}{\rho \cdot \left(\frac{A_{\text{upstream}}^2}{A_{\text{downstream}}^2} - 1 \right)}} \tag{11}$$

$\dot{V}_{\text{theoretical}}$ must be corrected for the flow rate dependencies of the cross-sectional areas A_{upstream} and $A_{\text{downstream}}$ and for the error made through the parametrization described in Equation 10. This parametrization only holds true, if uniform flow is given. Since fluid in contact with the tube walls experiences frictional forces due to viscosity, a velocity gradient develops across the tube's cross-section that needs to be corrected for (Bentley, 2005). This leads to a new expression for $\dot{V}$ with

$$\dot{V}_{\text{literature}} = C \cdot E \cdot A_d \cdot \sqrt{\frac{2 \cdot \Delta P}{\rho}} \tag{12}$$

and

$C =$ Discharge coefficient [-]
$\beta =$ Diameter ratio $= \frac{d}{D}$ [-]
$E =$ Velocity of approach factor $= \frac{1}{\sqrt{1-\beta^4}}$ [-]

A correction factor called the coefficient of discharge C is introduced that is a function of the diameter ratio β, the type of constriction as well as the Reynolds number Re_D. The Reynolds Number is a dimensionless number that delineates the ratio of inertial forces to viscous forces and is defined as followed (Bentley, 2005):

$$\text{Re}_D = \frac{v \cdot D \cdot \rho}{\mu} \tag{13}$$

with

$\mu =$ Dynamic fluid viscosity [Pa s]

Re_D describes whether flow is laminar or turbulent. Flow is considered to be laminar for $\text{Re}_D < 2000$, transitional for $2000 < \text{Re}_D < 4000$ and turbulent for $\text{Re}_D > 4000$ (Bentley, 2005). C has been determined experimentally for different types of constrictions, diameter ratios β and values for Re_D, resulting in the following empiric

equation, called the Stolz equation (Stolz, 1978) with

$$C = 0.5959 + 0.0312 \cdot \beta^{2.1} - 0.184 \cdot \beta^8 + 0.0029 \cdot \beta^{2.5} \cdot \left(\frac{10^6}{\mathrm{Re_D}}\right)^{0.75} \quad (14)$$

$$+ 0.0900 \cdot L_1 \cdot \beta^4 (1 - \beta^4)^{-1} - 0.0337 \cdot L_2' \cdot \beta^3$$

and $L_1 = L_2' = \frac{25.4}{D_{\mathrm{mm}}}$ for a flange tappings design. For Equation 12 to deliver accurate results, experimentally determined conditions of validity apply that are summarized in Table 1.

Table 1: Conditions of validity for a flange pressure tappings design (Bentley, 2005)

Parameter	Value range
d	≥ 12.5
D	50 - 760
β	0.2 - 0.75
$\mathrm{Re_D}$	$1260 \cdot \beta^2 \cdot D_{\mathrm{mm}}$ - 10^8

For the chimney of the MoHo v4.0, the pressure sensors are installed equidistantly next to the orifice plate (Figure 10 d). The orifice plate shows sloping edges of 45° on the downstream side to improve flow conditions (Figure 10 e). This approach is based on the so called flange pressure tappings design, which additionally delineates rules on sensor positions (Bentley, 2005). This flowmeter design is implemented into a vertically oriented chimney instead of a horizontal lying tube (Figure 7 c - e). Therefore, the spacing $l = 23.5$ mm between the orifice plate and each of the pressure sensors results in a difference in hydrostatic pressure of

$$\rho \cdot g \cdot (h_{\mathrm{downstream}} - h_{\mathrm{upstream}}) = 1.84 \, \mathrm{kg \, m^{-3}} \cdot 9.81 \, \mathrm{m \, s^{-2}} \cdot 0.047 \, \mathrm{m} \approx 0.85 \, \mathrm{Pa} \quad (15)$$

The value for the density ρ in Equation 15 is retrieved using Equation 1 and assuming a temperature of $T = 287.15$ K, a pressure of $p = 10^5$ Pa and a gas composition of 100 % CO_2. Because a pressure difference of 0.85 Pa falls within the measurement uncertainty of the MoHo flowmeter, this difference is assumed to be negligible. The lack of any moving parts makes this differential pressure based flowmeter design robust, reliable and easy to maintain, addressing the key problems with the previous cup anemometer design (Bentley, 2005). Furthermore, since the upstream pressure sensor has direct access to the chimney through the pressure tapping (Figure 8 c, Figure 10 a) rather than indirectly as in the previous design (Figure 5 b, c), changes in pressure and therefore the volumetric flowrate can be recorded in higher resolution. This presents the opportunity to more closely examine the cyclic eruptions and flow rate anomalies of the mofetta.

3.4 Sensors

3.4.1 Bosch BMP384

As already described in subsection 3.2, two absolute pressure sensors are installed for the differential pressure flowmeter instead of one differential pressure sensor. This was done due to the lack of commercially available low-cost differential pressure sensors that are pre-mounted onto a printed circuit board and provide differential pressure values at the level of resolution required for the flowmeter.

Since both pressure sensors have direct access to the chimney (Figure 8 c, Figure 10 a), they need to withstand high humidity conditions. The Bosch BMP384 pressure sensor (Figure 9 c) was chosen due to its gel-filled cavity that allows for high robustness against water (Bosch Sensortec GmbH, 2020) and its good performance under relevant operating conditions (Table 2). The version by SparkFun Electronics (Figure 9 a, b) was selected due to the standardized 2.54 mm connector pin spacing, allowing for a non-permanent jumper wire connection and therefore an efficient exchange of the pressure sensors in case of malfunction (Figure 9 e).

The Bosch BMP384 implements a piezo-resistive pressure sensing element (Bosch Sensortec GmbH, 2020). Typically, in this kind of sensor, the sensing element comprises of a Wheatstone bridge consisting of silicon piezoresistors mounted on top of a diaphragm. The diaphragm flexes in response to positive or negative pressure. When flexing, bending stresses are induced in the piezoresistors that translate into a fluctuation in resistance due to the piezoresisitve effect. The variation in resistance leads to a measurable change in output voltage if the Wheatstone bridge supplies the input voltage (Tran et al., 2018).

Table 2: Performance of Bosch BMP384 pressure sensor (Bosch Sensortec GmbH, 2020)

Parameter	Condition	Technical data
Absolute accuracy	300 - 1100 hPa & -20 - 65 °C	$\pm$ 0.65 hPa
	900 - 1100 hPa & 25 - 40 °C	$\pm$ 0.5 hPa
Temperature offset	700 - 1100 hPa & -20 - 0 °C	$\pm$ 2.6 Pa K^{-1}
	700 - 1100 hPa & 0 - 55 °C	$\pm$ 1.9 Pa K^{-1}
Long therm stability	12 months	$\pm$ 0.70 hPa
Maximum sampling rate	-	200 Hz

The downstream Bosch BMP384 was chosen to provide pressure data for Equation 3 due to its location closest to the Sensirion SEK-STC31 (Figure 7).

3.4.2 Thermistor

The thermistor (Figure 7 b, Figure 8 a) is a resistance thermometer made out of platin. The measurement principle is based on the temperature dependency of the electrical resistance R, which is approximately linearly dependent on the temperature T for certain temperature ranges (Foken, 2021):

$$R(T) = R(0\,^\circ\text{C}) \cdot (1 + \alpha \cdot T) \tag{16}$$

with
R = Electrical resistance [Ω]
T = Temperature [K]
α = Temperature coefficient of resistance [K^{-1}]

The thermistor used for the MoHo was calibrated against the EdgeTech RHCAL relative humidity calibration chamber by Büchau et al. (2023) and showed an electrical resistance of $R \approx 1620\,\Omega$ at $0\,^\circ\text{C}$, a coefficient of $\alpha > 0$ and a mean average error of 0.1 K. A positive value range for α means that the electrical resistance rises with the temperature (Foken, 2021).

3.4.3 Sensirion SHTC3

As part of the Sensirion SEK-STC31 (Figure 7 f, Figure 8 d - f), the Sensirion SHTC3 (Figure 8 f) measures the relative humidity capacitively (Sensirion AG, 2020a). Capacitive relative humidity sensors typically utilize a sensing element that is based on a small-sized capacitor with a humidity-sensitive material acting as a dielectric (Farahani et al., 2014). The electrical capacity C [F] of a capacitor is defined as

$$C = \epsilon_0 \cdot \epsilon_r \cdot \frac{A}{d} \tag{17}$$

with
ϵ_0 = Permittivity of vaccum [F m^{-1}]
ϵ_1 = Relative permittivity [-]
A = Surface area of plate [m^2]

and d being the plate spacing in meters (Bird, 2010). The higher the relative humidity, the more water is absorbed by the dielectric, the bigger the relative permittivity ϵ_1 and therefore the higher the capacity C. The change in capacity translates into a measurable change in voltage (Foken, 2021).

Additionally, the SHTC3 measures the temperature through the inclusion of a bandgap

sensing element (Sensirion AG, 2020a). These kind of sensors are based on the temperature characteristics of semiconducting junctions that are integrated into the interface circuit of the microchip. The energy gap, or bandgap, between the valence and conduction band of a semiconducting material changes with temperature in an inverse proportional manner (Wang, 2005).

The performance of the SHTC3 was tested by Büchau et al. (2023) through verification against the EdgeTech RHCAL relative humidity calibration chamber. A mean average error of 0.6 K for the temperature and 1.6 percent points for the relative humidity detection was determined (Büchau et al., 2023).

3.4.4 Sensirion STC31

Also part of the Sensirion SEK-STC31 (Figure 7 f, Figure 8 d - f) is the name giving STC31 CO_2 sensor (Figure 8 e). It works based on a thermal conductivity measurement principle (Sensirion AG, 2020b). The general principle behind this method is that a temperature difference exists between a hot and cold element through which heat transfer is established. A change in gas concentration or composition leads to a change in thermal properties and therefore a measurable change in heat transfer between the sensor elements (Gardner et al., 2023).

The STC31 needs to be configured to one of four predefined, assumed gas mixtures (Table 3). Being closest to the conditions within the chimney, CO_2 in air with a value range of 0 to 100 vol% CO_2 has been selected. Since the temperature, relative humidity and pressure influence the thermal conductivity, these values need to be measured and communicated to the STC31 in order for the sensor to perform corrections before providing CO_2 concentration data (Sensirion AG, 2020b). Both the temperature and relative humidity are provided by the SHTC3 (Figure 8 f) while the pressure is supplied by the downstream Bosch BMP384 (Figure 8 c, Figure 9 c).

Table 3: Performance of Sensirion STC31 CO_2 sensor (Sensirion AG, 2020b)

Parameter	Condition	Technical data
Gas mixture	0 to 100 vol% CO_2	CO_2 in N_2
	0 to 100 vol% CO_2	CO_2 in air
	0 to 25 vol% CO_2	CO_2 in N_2
	0 to 25 vol% CO_2	CO_2 in air
Accuracy	0 - 100 vol%	1 vol% + 3 % measured value
Temperature stability	Fulfilled by 90 % of sensors	0.025 vol% per °C
Measurement time	-	max. 66 ms

3.5 Calibration of Differential Pressure Flowmeter

As an alternative to the flow rate derivation method delineated in subsection 3.3, an additional calibration approach is utilized for the MoHo flowmeter. For this, similar to the flow rate calibration method implemented by Büchau et al. (2023) for the MoHo v3.2, a calibration with LTG 227VM-05 volumetric flow sensor was tested for the differential pressure flowmeter. The precision of the LTG 227VM-05 as a reference device was insufficient however, due to the slowness and fluctuation of the achievable volumetric flow rate conditions as well as the need for data acquisition through manual reading. For the fast-measuring Bosch BMP384 pressure sensors, an alternative approach for deriving a flow rate formula is utilized by building upon the concept of the bag experiments introduced by Büchau et al. (2023).

3.5.1 Orifice Plate

To find the most suitable orifice plate, plates of differing inner diameters d have been tested in the field under the pressure conditions of the mofetta with a simplified chimney setup based on segments of MoHo v3.2 (Figure 11 a). The pressure sensors are glued to the inside wall of two chimney segments (Figure 11 b) while an orifice plate is clamped in between the connection mechanism (Figure 11 c). Since this setup only serves as a temporary solution, the 14 mm by 22 mm manufacture printed circuit board (Figure 11 d) of the Bosch BMP384 was used instead of the one by SparkFun Electronics (Figure 9 a, b). Because the calibration can only be done without the roof segment, measurements with and without it have been taken to assess whether differential pressure conditions within the chimney are affected significantly.
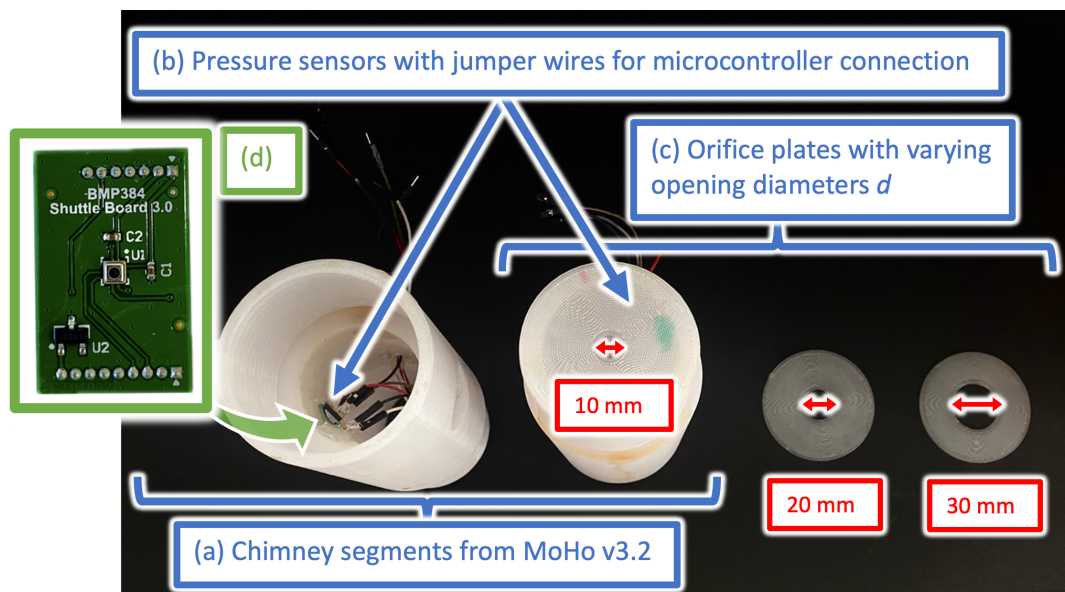

Figure 11: Simplified chimney setup for differential pressure flowmeter based on MoHo v3.2 PETG segments.

3.5.2 Balloon Experiments

To achieve a sufficient and robust calibration, the integrated differential pressure is calibrated against a finite, well-estimated volume that is filled within a known time window. A spherical metallic foil balloon with a diameter d_{Balloon} and circumference U is used as the reference volume. By measuring the balloon's circumference U during full expansion and assuming the it to be spherical, its volume V_{balloon} can be approximated as:

$$V_{\text{balloon}} = \frac{4}{3} \cdot \pi \cdot \left(\frac{d_{\text{Balloon}}}{2} \right)^3 = \frac{U^3}{6 \cdot \pi^2} \tag{18}$$

For a calibration experiment ("balloon experiment"), the chimney segment is replaced by a lid segment that allows for the placement of the balloon, that has been modified with a size-matching PLA end piece (Figure 12). The balloon is crumpled completely in order to achieve a balloon volume of $V_{\text{balloon}} = 0$ L. A balloon experiment starts as soon as the balloon is placed on top of the lid (Figure 12 a), allowing the exhaled gas to fill up the balloon (Figure 12 b, c). Since the balloon presents a hindrance to the upstreaming gas in this crumpled state, both pressure sensor signals are expected to show a significant and instantaneous increase before gradually falling again due to balloon expansion. As soon as the balloon is filled up completely (Figure 12 d), both the up- and downstream pressure sensor signals are expected to again show a significant and immediate peak, marking the end of the experiment. The time of the first pressure peak presents the start time t_{start} and the time of the second pressure peak marks the end time t_{end} of the time window, over which the balloon volume has been filled completely. Both t_{start} and t_{end} can now be determined graphically through the corresponding peaks in the pressure timeseries.
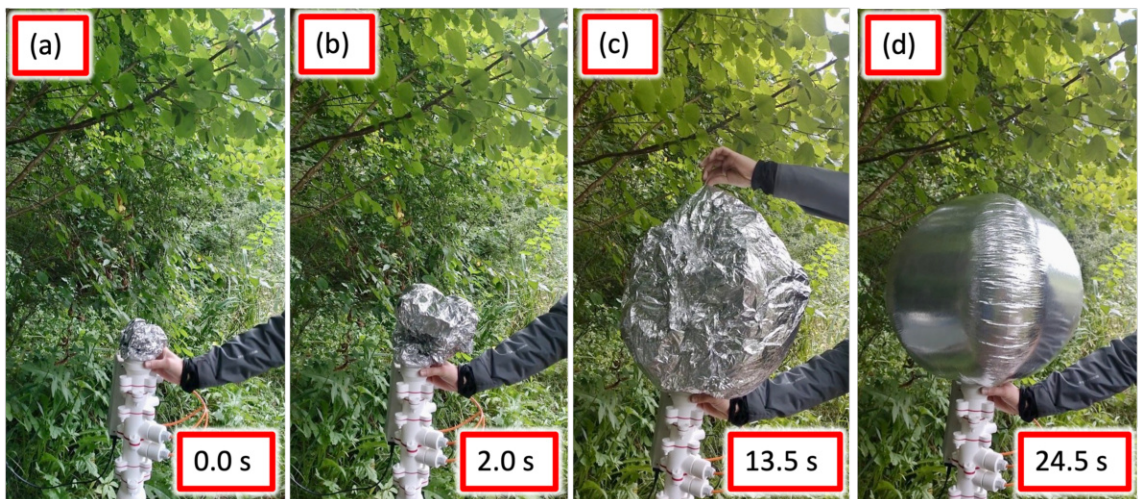

Figure 12: Balloon experiment with a foil balloon of the volume $V_{\text{balloon, 2}} = 69$ L. Divided into start time t_{start} (a), time of balloon expansion (b, c) and end time t_{end} (d). Taken by Yann Büchau on the 9th of August 2023. Time stamps in seconds since t_{start}.

A mean volumetric flow rate $\overline{\dot{V}}_{\text{balloon}}$ can be calculated through dividing the balloon volume V_{balloon} by the time difference $\Delta t = t_{\text{end}} - t_{\text{start}}$:

$$\overline{\dot{V}}_{\text{balloon}} = \frac{V_{\text{balloon}}}{\Delta t} \tag{19}$$

To account for variations in the volumetric flow rate $\dot{V}$ and to minimize systematic biased errors made when crumpling and placing the balloon, multiple experiments are taken. Based on the conservative maximum error estimation approach utilized by Büchau et al. (2023), equations for the maximum absolute error $\Delta\overline{\dot{V}}_{\text{balloon, abs}}$ and maximum relative error $\Delta\overline{\dot{V}}_{\text{balloon, rel}}$ [%] of $\overline{\dot{V}}_{\text{balloon}}$ are derived. Both equations have been obtained using the co2project python package created by Büchau (2023a). The equations account for the propagation of the maximum volume estimation error ΔU_{max} made through measuring the circumference U and the propagation of the maximum graphical estimation error $\Delta t_{\text{start, max}}$ for t_{start} and $\Delta t_{\text{end, max}}$ for t_{end} with

$$\Delta\overline{\dot{V}}_{\text{balloon, abs}} = \frac{U^3 \Delta t_{\text{start, max}} \frac{1}{|t_{\text{start}} - t_{\text{end}}|^2}}{6\pi^2} + \frac{U^3 \Delta t_{\text{end, max}} \frac{1}{|t_{\text{start}} - t_{\text{end}}|^2}}{6\pi^2} + \frac{U^3 \Delta U_{\text{max}} \frac{1}{|t_{\text{start}} - t_{\text{end}}|}}{2\pi^2} \tag{20}$$

and

$$\Delta\overline{\dot{V}}_{\text{balloon, rel}} = \frac{\Delta\overline{\dot{V}}_{\text{balloon, abs}}}{\overline{\dot{V}}} \tag{21}$$

A function that calculates the volumetric flow rate $\dot{V}$ from a given value for the pressure difference ΔP is retrieved through an optimization approach. First, a power law with two parameters, a $[\text{L s}^{-1}\,\text{Pa}^{-1}]$ and b [-], is defined. It fullfills both the nonlinear relationship delineated by Equation 12 as well as the boundary condition of $\Delta P = 0\,\text{Pa}$ translating into a volumetric flow rate of $\dot{V} = 0\,\text{L s}^{-1}$:

$$\dot{V} = \text{sign}(\Delta P) \cdot \text{a} \cdot |\Delta P|^{\text{b}} \tag{22}$$

If b < 1 and $\Delta P < 0\,\text{Pa}$, the root of a negative value is taken, resulting in a complex number. To prevent errors from emerging during optimization because of this, the absolute value of ΔP is taken while the sign is preserved through a sign-function (Equation 22). This also makes the function point-symmetric, which is assumed to be true and allows to quantify the flow rate $\dot{V}$ during suction events of the mofetta like the ones that were observed by Büchau et al. (2023).

An optimization method calls a cost-function with varying values for a and b. Within this cost-function, a volume error of

$$\text{error} = |(V_{\text{balloon}} - V_{\text{calculated}})| \tag{23}$$

between the balloon volume V_{balloon} and a calculated volume $V_{\text{calculated}}$ is determined for each of the N experiments. The calculated volume $V_{\text{calculated}}$ is retrieved by integrating a determined value for the flow rate $\dot{V}$ over a corresponding time interval $t_2 - t_1$ using the trapezoidal rule (NumPy Developers, 2022):

$$V_{\text{calculated}} = \int_{t_1}^{t_2} \dot{V}(t)\,\mathrm{d}t \approx (t_2 - t_1) \cdot \frac{1}{2}\left(\dot{V}(t_1) + \dot{V}(t_2)\right) \tag{24}$$

The average of theses volume errors then presents the scalar return value of the cost-function. Several optimization methods are applied and the best one is retained for further use (The SciPy community, 2023).

3.6 Data Processing & Acquisition

For the finalized MoHo v4.0 setup, all sensors are connected to an ESP8266EX micro-controller that is mounted onto a Wemos D1 mini Pro module. The module is part of a custom circuit board located in the electrical enclosure box (Figure 7). Sensor communication happens through the **I**nter-**I**ntegrated **C**ircuit (**I^{2}C**) communication protocol. All sensor outputs need to be queried sequentially before the CO_2 mass flux is calculated on-board since the ESP8266EX is limited to single-core processing and due to the serial communication through I^{2}C. Data is then transmitted wire-lessly through a **W**ireless **L**ocal **A**rea **N**etwork (**WLAN**) that is established by a central station via the **M**essage **Q**ueuing **T**elemetry **T**ransport (**MQTT**) messaging protocol (Büchau et al., 2022). Data is published at a lowered rate 0.5 Hz and then uploaded to the server of the University of Tübingen through a cellular network. For balloon experiments, publishing through MQTT is temporarily deactivated. Instead, pressure data is obtained through a USB interface for a higher temporal resolution.

Since both pressure sensors show signal noise and temperature drift of varying inten-sity, their combined effect is reflected in the pressure difference values. Both in the lab and field, this resulted in volumetric flow rates of $\dot{V} > 0\ \text{L s}^{-1}$ under zero flow rate conditions. To counteract this, a zero offset correction is implemented. Differ-ent metrics based on the standard deviations of the up- and downstream pressure sensor signals have been tested in the lab. Different CO_2 concentration conditions were achieved by manually injecting CO_2 through a gas bottle while the flow rate conditions were altered with bursts of pressurized nitrogen. However, the mofetta hood conditions could not be accurately simulated, causing the tested metrics to wrongly correct derived values for the flow rate back to $0\ \text{L s}^{-1}$ under significant flow rate conditions. Therefore, a zero offset correction with a correction value is implemented instead. The correction value is determined by exposing the MoHo to

no flow conditions and then taking the mean pressure difference between up- and downstream sensor of that time frame. Half of this value is then subtracted from each of the raw upstream pressure values while half of this value is added to each of the raw downstream values. This causes the signals to match under no flow conditions. Then, as already touched upon in subsection 3.1, a moving mean is taken. For this, an array spanning 100 elements is filled continuously with the latest 100 values of both pressure sensor outputs. The mean of an array is taken everytime a value is replaced. This is done in order to reduce the effects of signal noise.

4   Results

4.1   Calibration of Differential Pressure Flowmeter

4.1.1   Orifice Plate

An orifice plate with an opening diameter $d = 10$ mm presented too much of a resistance for the upstreaming gas as for them to be channeled through and out of the chimney. Instead, the majority of the CO_2 masses degassed from points adjacent of plastic barrel. An orifice plate with an inner diameter of $d = 30$ mm allowed the gas to be channeled through the chimney. However, the pressure difference values between the up- and downstream pressure sensors were too small compared to the signal noise in order for useful calibration experiments to be taken (Table 4). An orifice plate with $d = 20$ mm achieved the highest pressure difference values whilst also channelling the gas through the chimney (Table 4). The presence of the roof segment does not change the differential pressure values significantly, making its influence on the pressure conditions present within the chimney negligible (Table 4).

Table 4: Comparison of the mean differential pressure $\overline{\Delta P}$ for differing inner diameters d of the orifice plate and varying roof conditions. Taken on the 17$^{\text{th}}$ of May 2023 on top of the mofetta with a temporal resolution of 10 Hz.

Inner diameter d [mm]	Condition	Duration [min]	$\overline{\Delta P}$ [Pa]
30	No roof	9	(39.25 ± 32.53)
30	With Roof	26	(38.18 ± 29.92)
20	No roof	5	(187.83 ± 35.88)
20	With Roof	4.5	(188.56 ± 37.70)

4.1.2   Balloon Experiments

Two balloons of differing estimated circumferences U and volumes V_{balloon} have been used (Table 5). These balloons have been chosen since they were the the biggest

commercially available foil balloons at the time. Due to their simple geometric shape, the relative errors of both balloon volume estimations are significantly smaller than the ones for the trash bags used for calibration experiments by Büchau et al. (2023) described in subsection 2.3 (Table 5).

Table 5: Comparison of estimated circumference U, volume V_{balloon} and relative error for V_{balloon} of the two balloons utilized for the calibration experiments. Volume estimations (V_{bag}) & relative errors for the trash bags used for calibration of the MoHo v3.2 by Büchau et al. (2023) are added for comparison.

Balloon No.	Circumference U [cm]	Volume V_{balloon} [L]	V_{balloon} relative error [%]
1	(143 ± 5)	(49 ± 5)	± 10.2
2	(160 ± 2)	(69 ± 3)	± 4.3
Bag No.	Shape	Volume V_{bag} [L]	V_{bag} relative error [%]
1	Irregular	(50 ± 20)	± 40
7	Irregular	(60 ± 20)	± 33

The $V_{\mathrm{balloon,\,1}} = 49$ L balloon was used for $N = 9$ experiments on the 02.07.2023 with the simplified chimney setup (Figure 11), further referred to as "calibration no. 1". The pressure and differential pressure timeseries for one of those balloon experiments are displayed in Figure 13.
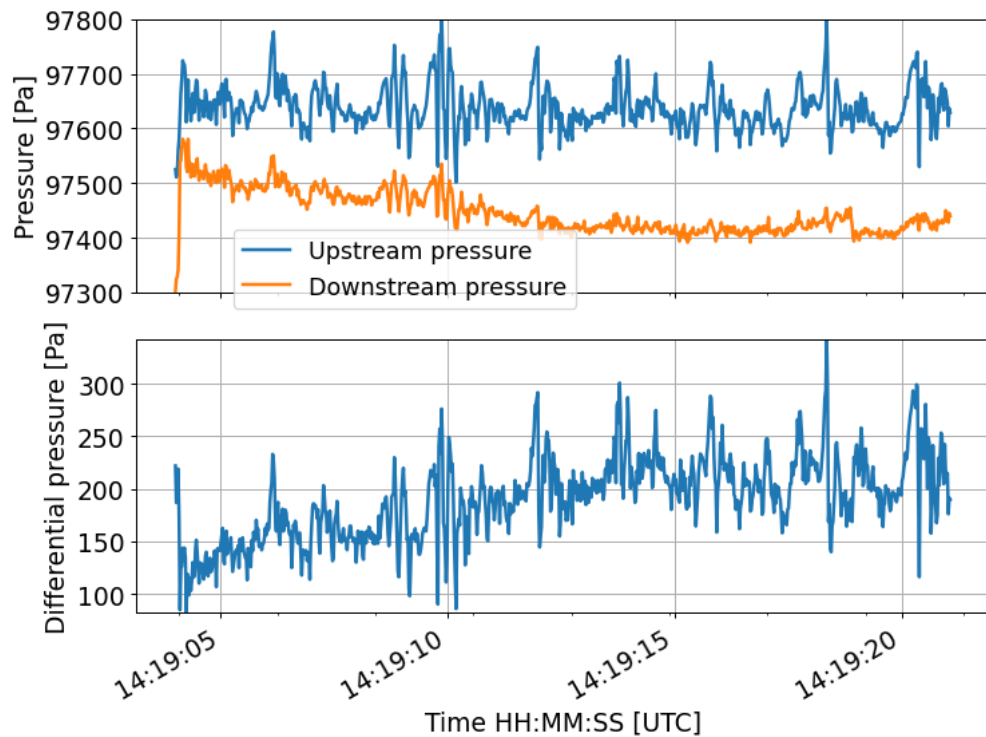

Figure 13: Pressure & differential pressure for the 4th balloon experiment of calibration no. 1 ($V_{\mathrm{balloon,\,1}} = 49$ L). Temporal resolution resampled to 50 Hz.

The mean flow rate $\overline{\dot{V}}_{\text{balloon}}$, corresponding absolute ($\Delta\overline{\dot{V}}_{\text{balloon, abs}}$) and relative maximum error ($\Delta\overline{\dot{V}}_{\text{balloon, rel}}$) and the minimum ($\Delta P_{\text{min}}$) and maximum ($\Delta P_{\text{max}}$) differential pressure for each of the N experiments are seen in Table 6. Pressure values were taken at a temporal resolution of 100 Hz.

Table 6: Mean volumetric flow rate $\overline{\dot{V}}_{\text{balloon}}$, corresponding absolute maximum error $\Delta\overline{\dot{V}}_{\text{balloon, abs}}$ and relative maximum error $\Delta\overline{\dot{V}}_{\text{balloon, rel}}$ as well as minimum differential pressure ΔP_{min} and maximum differential pressure ΔP_{max} for all balloon experiments of the 1st calibration ($V_{\text{balloon,1}} = 49$ L).

No.	$\Delta\mathbf{P}$ [Pa]		$\overline{\dot{\mathbf{V}}}_{\mathbf{balloon}}$ [L s^{-1}]	$\Delta\overline{\dot{\mathbf{V}}}_{\mathbf{balloon}}$	
	min	max		abs [L s^{-1}]	rel [%]
1	73	348	3.07	0.35	11.42
2	109	374	3.02	0.37	12.08
3	75	336	2.79	0.34	12.13
4	82	342	2.89	0.37	12.71
5	31	272	2.48	0.30	12.10
6	52	313	2.98	0.36	12.06
7	14	313	2.57	0.31	12.15
8	-9	274	2.53	0.30	11.82
9	47	305	2.85	0.36	12.68
Mean	51	307	2.80	0.34	12.13

The optimization results depend on the pre-determined guessed start values for the parameters a and b, the chosen algorithm as well as the distribution and abundance of pressure difference values across balloon experiments. For the 1st calibration, the Nelder-Mead method (Nelder & Mead, 1965) resulted in the lowest error of 0.48 L for a $= 0.05002$ L s^{-1} Pa^{-1} and b $= 0.7727$. For the used balloon of the volume $V_{\text{balloon,1}} = 49$ L, this represents a relative error of $\sim 1\,\%$. Flow rates have been derived through the power law (Equation 22) with these values for a and b and the differential pressure ΔP during three of the balloon experiments (Figure 14).

The balloon with the volume $V_{\text{balloon, 2}} = 69$ L was used for $N = 5$ experiments with the finalized chimney flowmeter (Figure 10) on the 09.08.2023, further referred to as "calibration no. 2". Pressure values were again taken at a temporal resolution of 100 Hz. The mean flow rate $\overline{\dot{V}}_{\text{balloon}}$, corresponding absolute ($\Delta\overline{\dot{V}}_{\text{balloon, abs}}$) and relative maximum error ($\Delta\overline{\dot{V}}_{\text{balloon, rel}}$) and the minimum ($\Delta P_{\text{min}}$) and maximum ($\Delta P_{\text{max}}$) differential pressure for each of the N experiments are summarized in Table 7.
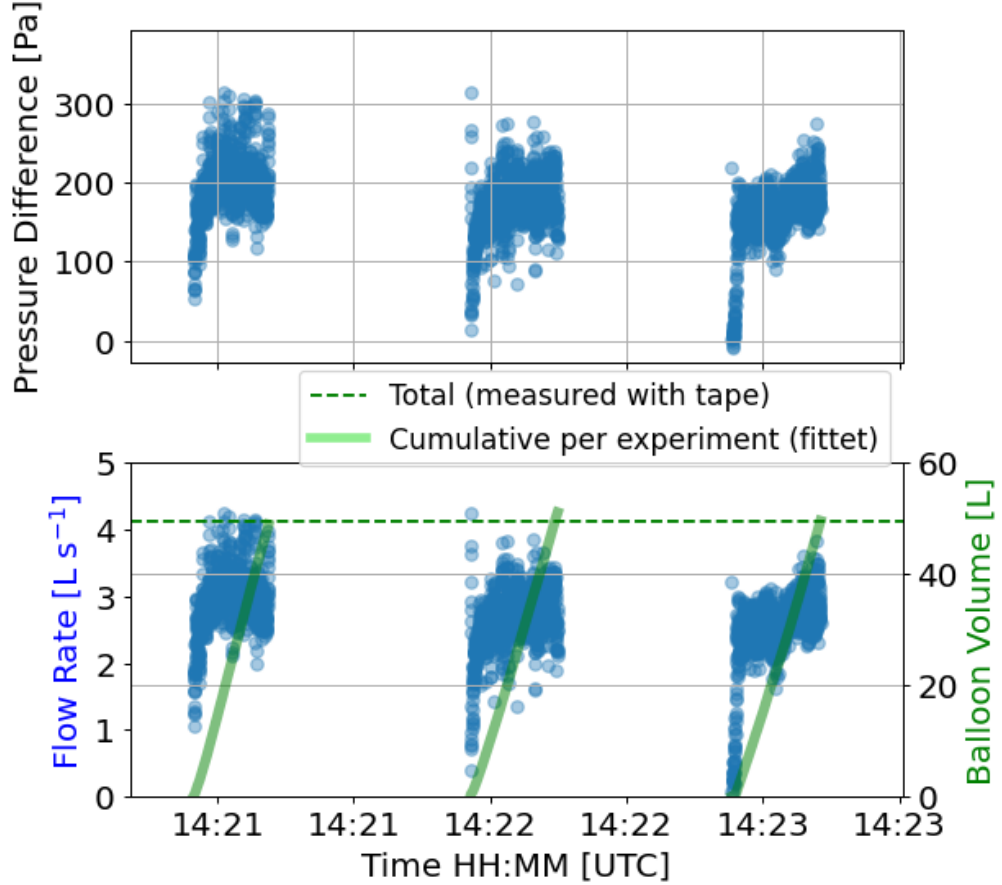
Figure 14: Differential pressure, derived volumetric flow rates and cumulative volume per experiment for balloon experiments 6 to 8 of the 1st calibration ($V_{\text{balloon, 1}} = 49$ L). Resampled to a temporal resolution of 50 Hz.

Table 7: Mean volumetric flow rate $\overline{\dot{V}}_{\text{balloon}}$, corresponding absolute maximum error $\Delta\overline{\dot{V}}_{\text{balloon, abs}}$ and relative maximum error $\Delta\overline{\dot{V}}_{\text{balloon, rel}}$, minimum differential pressure ΔP_{min} and maximum differential pressure ΔP_{max} for all balloon experiments of the 2nd calibration ($V_{\text{balloon, 2}} = 69$ L).

No.	ΔP [Pa]		$\overline{\dot{V}}_{\text{balloon}}$ [L s^{-1}]	$\Delta\overline{\dot{V}}_{\text{balloon}}$	
	min	max		abs [L s^{-1}]	rel [%]
1	97	299	2.92	0.18	6.07
2	140	424	2.89	0.17	5.84
3	6	362	2.89	0.16	5.42
4	116	337	2.88	0.17	5.83
5	11	338	2.92	0.19	6.49
Mean	74	352	2.90	0.17	5.93

Compared to the 1st calibration (Table 6), the balloon experiments of the 2nd calibration include less differential pressure values within the realm close to $\Delta P = 0$

Pa (Table 7). This is due to the decreased resistance placed on the upstreaming gas by the higher-volume balloon and due to natural variations in flow rate of the mofetta. This results in a power law function with optimized parameter values that likely overestimates small values for ΔP. By only choosing balloon experiments 2,3 and 5 that span across the widest value range for ΔP (Table 7), this issue can be minimized. Through Powell's conjugate direction method (Powell, 1964), this leads to an error of 3.07 L and values of a = 0.07410 L s^{-1} Pa^{-1} and b = 0.7000. For the balloon with the volume $V_{\text{balloon, 2}} = 69$ L, this represents a relative error of $\sim 4.4\,\%$.

As delineated by Equation 20, the absolute maximum error $\Delta \overline{\dot{V}}_{\text{balloon, abs}}$ of the mean volumetric flow rate $\overline{\dot{V}}$ for a balloon experiment decreases with a rise in Δt and drop in ΔU_{max}. By switching from the 1$^{\text{st}}$ balloon ($V_{\text{balloon, 1}} = 49$ L) to the 2$^{\text{nd}}$ balloon ($V_{\text{balloon, 2}} = 69$ L), the absolute maximum error $\Delta \overline{\dot{V}}_{\text{balloon, abs}}$ is decreased by half across all balloon experiments (Table 6, Table 7).

4.2 Comparison of Functions for the Volumetric Flow Rate

For the flowmeter of the MoHo v4.0, a diameter ratio of $\beta = 0.36$ and a velocity of approach factor E of 1.01 emerge. For comparison of the equation for practical use $\dot{V}_{\text{literature}}$ (Equation 12) described in subsection 3.3 with the power laws retrieved in subsubsection 4.1.2, the gas is assumed to be made out of 100 % CO_2, to have an average velocity of $v = 1$ m s^{-1} and a temperature of $T = 287.15$ K $= 14\,°$C. For a pressure of $p = 1$ bar $= 10^5$ Pa, a density of $\rho \approx 1.84$ kg m^{-3} (using Equation 1) and a dynamic viscosity of $\mu \approx 14.49 \cdot 10^{-6}$ Pa s emerge (Fenghour et al., 1998). This results in a Reynolds number of

$$\text{Re}_{55\,\text{mm}} = \frac{1 \text{ m s}^{-1} \cdot 0.055 \text{ m} \cdot 1.84 \text{ kg m}^{-3}}{14.49 \cdot 10^{-6} \text{ Pa s}} \approx 6984 \tag{25}$$

By implementing Equation 14 established by Stolz (1978), these values for $\text{Re}_{55\,\text{mm}}$ and β result in a discharge coefficient of $C = 0.61$. The equation for practical use $\dot{V}_{\text{literature}}$ with these values for C and E is visualized Figure 15 along with the power laws from calibration no. 1 and 2.

While the orifice plate's opening diameter $d = 20$ mm, inner chimney diameter $D = 55$ mm and diameter ratio β fall within the validity conditions delineated in Table 1, $\text{Re}_{55\,\text{mm}}$ does not meet the condition of $20584 \leq \text{Re}_{55\,\text{mm}} \leq 10^8$. Therefore, $\dot{V}_{\text{literature}}$ is not appropriate for the flow rate derivation for the MoHo v4.0. Nonetheless, its general shape and realm of flow rate conversion validate the balloon experiments as to a suitable calibration approach (Figure 15).
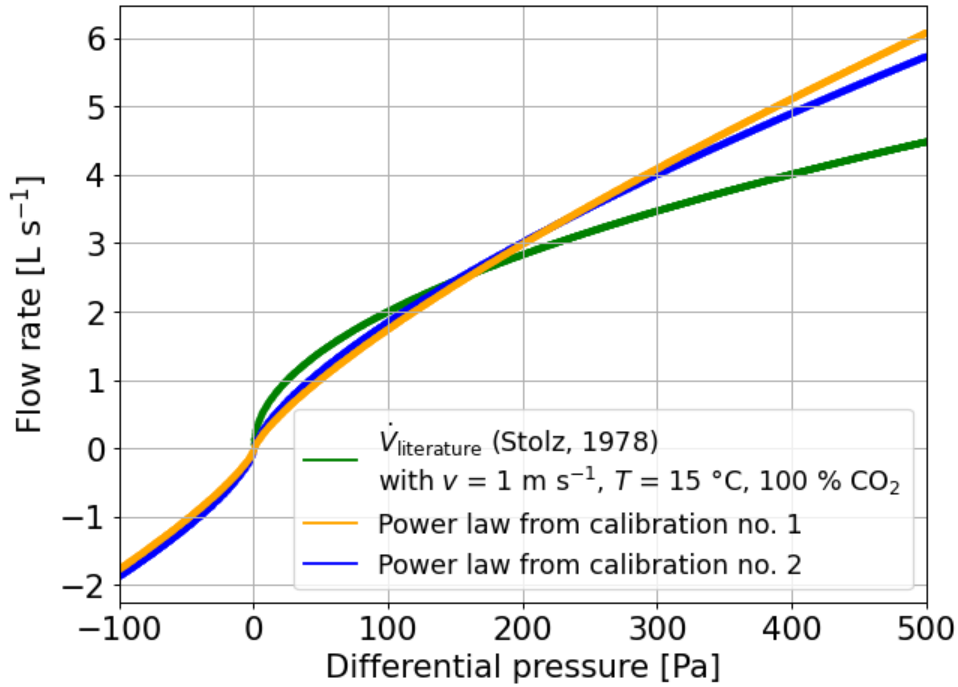
Figure 15: Power laws from balloon calibrations and equation for practical use $\dot{V}_{\text{literature}}$ applied onto a differential pressure range of -100 to 500 Pa

As mentioned in subsubsection 4.1.2, the optimization results are crucially influenced by the range and distribution of differential pressure data. For both calibrations, most of the differential pressure data was obtained for $\Delta P \approx 220$ Pa, leading to the same flow rate derivations and consequentially the intersection of both curves (Figure 15). The power law from calibration no. 1 is characterized by a more linear curve shape while the one from calibration no. 2 is slightly more square-root-like (Figure 15). This means the calibration no. 1 power law translates high values for ΔP into higher flow rates compared to the one from the 2nd calibration. On the other hand, the power law from calibration no. 2 translates low values for ΔP into slightly higher flow rates than the one from the 1st calibration. Since the flow rate derived through $\dot{V}_{\text{literature}}$ is proportional to the square root of the differential pressure ΔP (Equation 12), it translates high values for ΔP into significantly lower flow rates and small values for ΔP into substantially higher flow rates compared to both power laws (Figure 15). In the context of the differential pressure conditions characterizing the investigated mofetta, this dampened flow rate conversion for high values for ΔP makes the mofetta's cyclic eruptions less significant compared to the power laws (Figure 16).
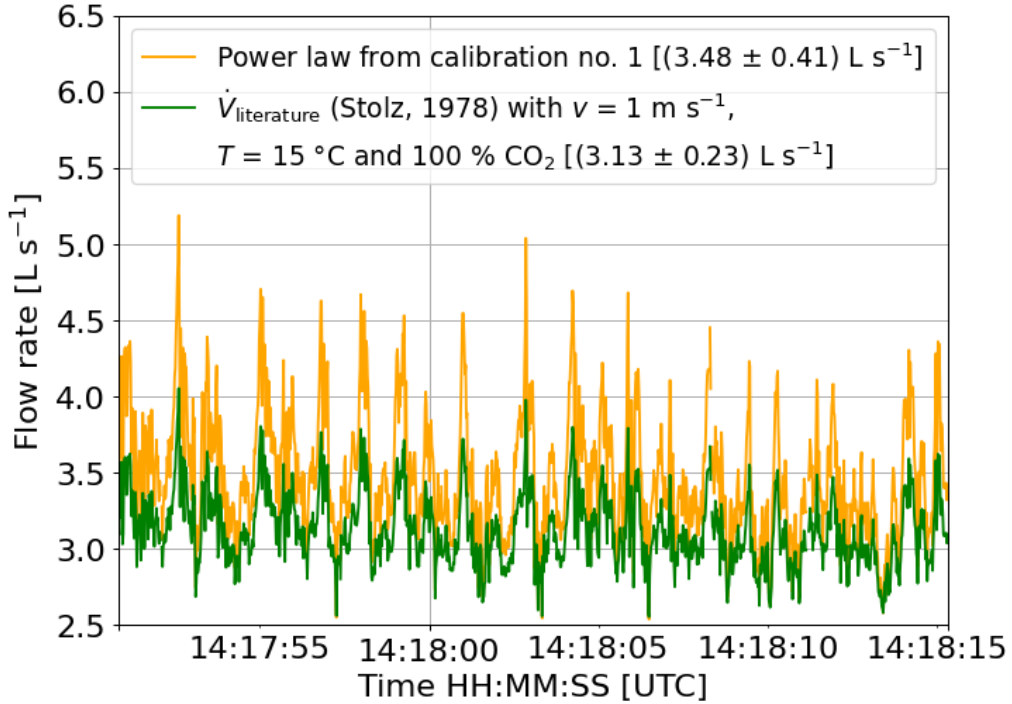
Figure 16: Calibration no. 1 power law and equation for practical use $\dot{V}_{\text{literature}}$ applied onto a differential pressure timeseries of the mofetta taken on the 2nd of June 2023. Resampled to a temporal resolution of 50 Hz.

Even if the conditions of validity were met for $\dot{V}_{\text{literature}}$, the power laws are more suitable for the flowmeter since these calibrations have been adapted for the specific MoHo chimney design and pressure conditions the mofetta. The point-symmetry of both power laws allows for negative flow rates and therefore for flow rate quantification if the mofetta sucks outside air into the chimney, which is not possible with $\dot{V}_{\text{literature}}$. The power law's more linear curvature, that leads to a translation of high values for ΔP into higher flow rates than compared to $\dot{V}_{\text{literature}}$, is more realistic since Büchau et al. ([2023](#)) measured flow rates of up to 6 L s^{-1} with MoHo v3.2's cup anemometer. Out of the two power laws, the one from the 1st optimization is assumed to be the more robust one due to its lower optimization error and larger number of balloon experiments spanning over a larger differential pressure range. This is why this power law will be used for the final MoHo v4.0 flowmeter:

$$\dot{V} = \text{sign}(\Delta P) \cdot 0.05002 \, \text{L s}^{-1} \, \text{Pa}^{-1} \cdot |\Delta P|^{0.7727} \tag{26}$$

4.3   Temporal Quantification of Cyclic Eruptions

The upstream pressure sensor's position close to the mofetta ([Figure 7](#) c) and direct access to the chimney ([Figure 10](#) a) allow for high resolution pressure data. Through a variance spectrum of this signal, the cyclic eruptions of the mofetta can be quantified ([Figure 17](#)).
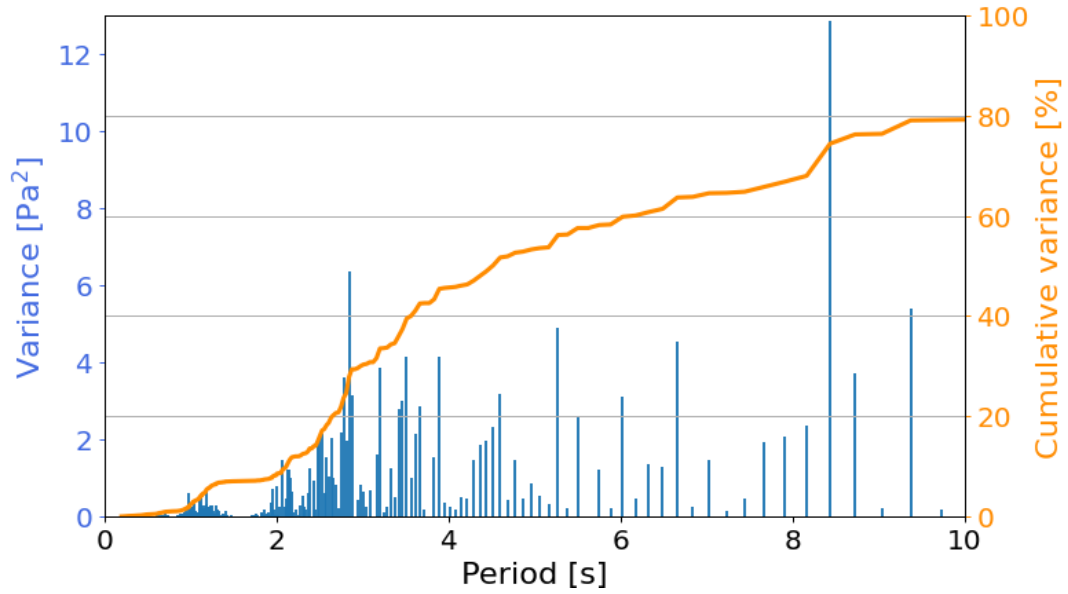
Figure 17: Variance spectrum of a 4 minute upstream pressure timeseries taken on the 9th of August 2023. The absolute and cumulative variance are shown for a period time of 0 to 10 seconds. The sum of the spectrum lies at 200.36 Pa^2 and the total variance at 200.38 Pa^2, fulfilling Parseval's theorem. Resampled to a temporal resolution of 100 ms.

Compared to the variance spectrum of a 60 minute flow rate time series measured by Büchau et al. (2023) in February of 2022, a new lower-period cycle at ~ 1 second emerges that accounts for $\sim 10\%$ of the total signal variance (Figure 17). For the flow rate spectrum, a dominant period window spanned across 3 - 5 seconds ("4-s-cycle") and was responsible for 57 % of the variance. This most prevalent window has now shifted slightly to the lower end of the spectrum to a 2 - 4 seconds window ("3-s-cycle") that accounts for $\sim 40\%$ of the variance (Figure 17). Periods in between 4 and 10 seconds are responsible for $\sim 30\%$ of the signal variance (Figure 17). Due to the short length of the pressure time series, lower frequencies than 0.1 Hz are less prevalent and therefore less relevant for the spectral variance of a 4 minute signal.

4.4 Zero Offset Correction & Data Transmission

For the 1st calibration, a correction value of 8 Pa was determined at the site just before before measurements on the mofetta were taken and then applied in post-processing. For the deployment of the MoHo, the correction value needed to be already implemented into the microcontroller code since the differential pressure values are directly used by the STC31 for internal corrections (subsubsection 3.4.4) and for calculations of the flow rate and the CO_2 mass flux (subsection 3.1). For this, attempts were made to quantify the long-term mean zero offset under isolated conditions in the lab by sealing both ends of the chimney and recording pressure difference

data for multiple days. Due to small temperature changes of $\pm$ 1 °C in the lab, a mostly positive relationship between temperature and differential pressure was revealed. This lead to a differential pressure signal shifting by $\pm$ 6 Pa, which is slightly more than the combined temperature offset of both sensors of $\pm$ 3.8 Pa according to manufacturer specifications (Table 2). A correction value of 23 Pa emerged.

On the 9th of August 2023, the final MoHo v4.0 setup was deployed on the mofetta for the first time. The recorded timeseries spans 35 minutes, after which publishing via MQTT stopped. It is suspected that this issue might related to data communication with the pressure sensors. This has occurred in the lab environment before and could only be resolved by forcibly disconnecting the sensors from the microcontroller. The code was not designed to handle a scenario where other sensors continue to publish data while the pressure sensors don't. Additionally, the code was not prepared to be remotely reprogrammed, as is the case with the rest of the network from Büchau et al. (2022). On this particular day, the correction value determined under isolated lab conditions proved to be unsuitable. Instead, the offset between pressure sensors was highly inconsistent when the MoHo v4.0 was taken off the mofetta. Since deployment of the MoHo happened right after the last balloon experiment, the correction value of that experiment was used in post-processing for the correction of the pressure signals. Therefore, it is assumed that the zero offset has not changed significantly within the following 35 minutes since the last balloon experiment. This assumption holds true considering the derived mean volumetric flow rate of $\sim$ 3.3 L s^{-1} (Figure 18) falls well within the measurement range of the 2nd of June 2023 (Figure 16).

4.5 Measurements of the 9th of August 2023

During its operation, the MoHo captured an event of significant volumetric flow rate $\dot{V}$ and CO_2 mass flux $\dot{m}_{CO_2}$ change (Figure 18). The flow rate $\dot{V}$ decreased from the previously steady level of 3.3 L s^{-1} to 2.7 L s^{-1} over the span of about 4 minutes (Figure 18). After that, the flow rate increased by $\sim$ 40 % to 3.8 Ls^{-1} over the course of 1 minute before falling again to a steady level of 2.7 Ls^{-1} within 3 minutes. Since the volumetric CO_2 concentration X_{CO_2} did not change significantly (Figure 18), the shift in CO_2 mass flux $\dot{m}_{CO_2}$ is mainly linked to the change in differential pressure ΔP and therefore the flow rate. The peak in differential pressure is attributed to a peak in pressure P of the upstream sensor while the downstream pressure does not show any substantial change (Figure 18). It is worth pointing out that the moving mean of the upstream pressure shows a more significant deviation during the anomaly compared to the raw values (Figure 18).
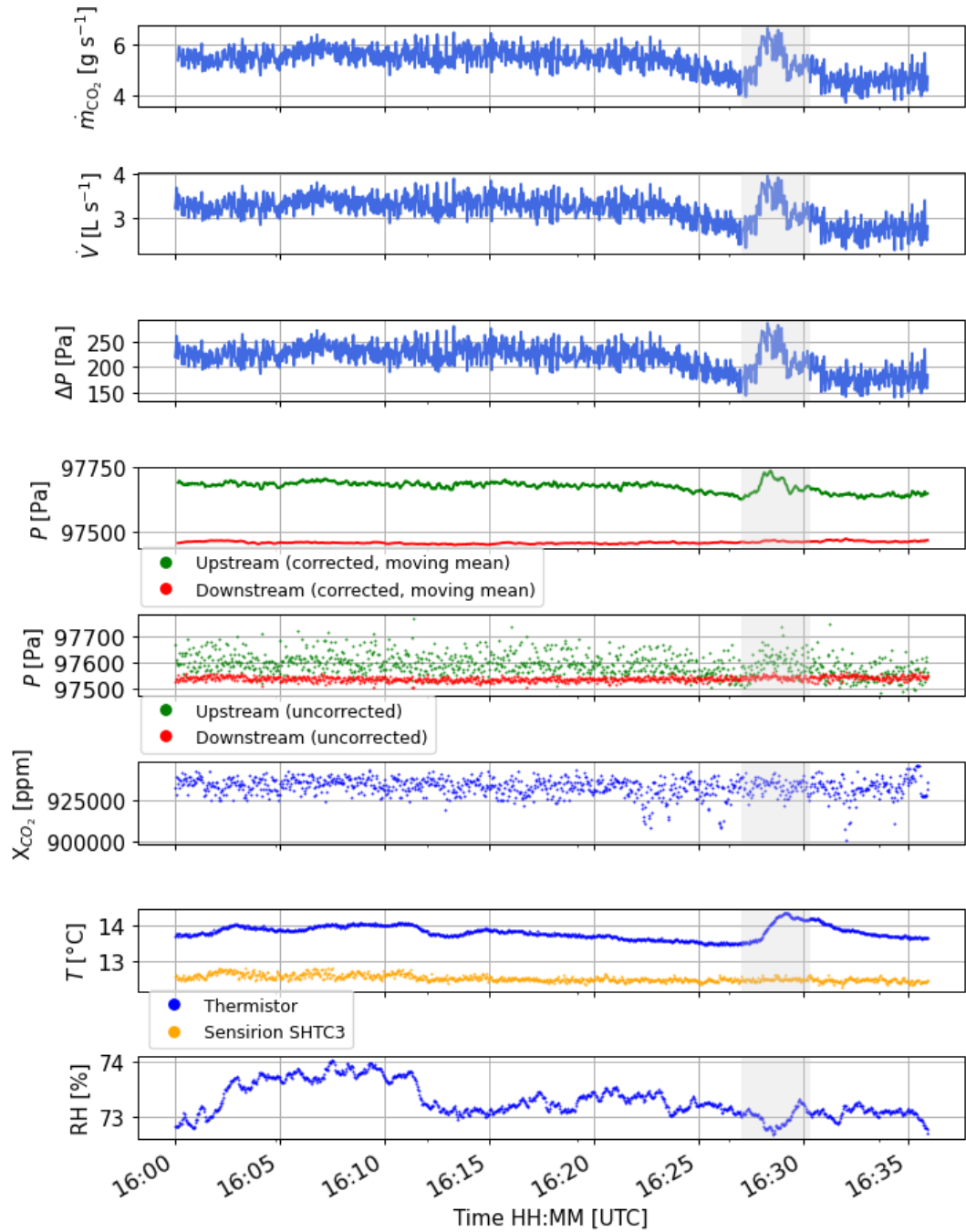
Figure 18: Measurements of MoHo v4.0 on the mofetta on the 9$^{\text{th}}$ of August 2023. Vertical grey line indicates time of flow rate & temperature anomaly.

It is unlikely that this event was caused by hard- or software errors of the pressure sensors. This is because the anomaly corresponds to a significant increase in temperature T of 0.8 K measured by the thermistor, a completely independent measurement system (Figure 18). The thermistor's reliability is validated by its synchronous behaviour to the Sensirion SHTC3 before the anomaly in between 16:00 and 16:15 pm (Figure 18). What is noticeable, is that the thermistor's temperature output already started to diverge from the Sensirion SHTC3's measurements at 16:15 pm with a

steady drop of 0.4 K until the rise in temperature $\sim$ 13 minutes later (Figure 18). The relative humidity RH did not change significantly during this event (Figure 18).

This anomaly shows key differences compared to the anomalies observed by Büchau et al. (2023) in February of 2022. During these events, the flow rate increase of $\sim$ 25 % was accompanied by a short significant reduction in CO_2 concentration of around 50 %. It then took about one day for the volumetric flow rate to drop back to the baseline recorded prior of the event. The thermistor measured a corresponding short drop in temperature of almost 2 K, which was likely due to the transportation of colder outside air into the chimney as the mofetta changed from inhaling to exhaling (Büchau et al., 2023). On the 9th of August 2023 however, the suction of outside air into the chimney did not happen since neither the downstream Bosch BMP384 pressure sensor nor the Sensirion SHTC3 showed any significant change in their respective outputs (Figure 18). What all events have in common is that the flow rate reduces right before the exhalation and the general realm by which the flow rate increases ($\sim$ 25 - 40 %).

5 Discussion

5.1 Measurements of the 9th of August 2023

It is worth making a feasibility assessment whether the rise in temperature T with the rise in pressure p can be explained by an increase in internal energy through adiabatic compression. This relationship is described through

$$p_{1,\text{ adiabatic}}^{1-\beta} \cdot T_{1,\text{ adiabatic}}^{\beta} = p_{2,\text{ adiabatic}}^{1-\beta} \cdot T_{2,\text{ adiabatic}}^{\beta} \tag{27}$$

and involves the heat capacity ratio β [-] (Atkins & Paula, 2006). For CO_2 at 0 °C, β is equal to 1.301 (Langeheinecke et al., 2013). By rearranging Equation 27, the temperature $T_{2,\text{ adiabatic}}$ that would theoretically result through adiabatic compression in the case of the anomaly can be obtained:

$$T_{2,\text{ adiabatic}} = \left(\frac{p_1^{1-\beta}}{p_2^{1-\beta}}\right)^{\frac{1}{\beta}} \cdot T_1 \approx 286.72\,\text{K} = 13.57\,^{\circ}\text{C} \tag{28}$$

with
p_1 = Pressure prior to anomaly = 97700 Pa
p_2 = Pressure at time of anomaly = 97800 Pa
T_1 = Temperature prior to anomaly = 286.65 K = 13.5 °C

In contrast, the temperature that was measured by the thermistor at the time of the anomaly is $T_2 = 287.45$ K $= 14.3$ °C. Even if adiabatic conditions were met, the rise in temperature cannot be attributed to adiabatic compression since T_2 is significantly higher than $T_{2,\,\text{adiabatic}}$. This suggests that the gas temperature increase is of geologic origin and is unlikely to have been caused by the presence of the measurement setup. The lack of temperature detection by the Sensirion SHTC3 compared to the thermistor may be explained by its position farther away from the mofetta in combination with its larger mean average error of 0.6 K compared to the thermistors mean average error of 0.1 K (Büchau et al., 2023).

These kinds of flow rate anomalies are usually linked to seismic activity in the form of local earthquakes that occur around the time of the anomaly and induce a change in fluid migration paths and reservoir discharge (Fischer et al., 2017). However, for the flow rate anomaly of the mofetta on the 9th of August 2023, no spacial and temporal corresponding earthquake(s) have been detected (LGRB, 2023), leaving room for speculation for the exact geologic cause.

5.2 Dynamics in Volumetric Flow Rate & Eruption Frequency

As summarized in Table 8, mean flow rates captured with the MoHo v4.0 during operation in summer of 2023 are $\sim$ 14 - 24 % higher compared to the value collected with the MoHo v3.2 in winter of 2022. This difference is unlikely be explained by diverging reproducibility between the two flow rate measurement techniques of MoHo v3.2 and v4.0 alone, since the mean flow rate across all balloon/bag experiments has changed significantly as well with an increase of $\sim$ 36 - 41 %.

Table 8: Comparison of flow rate measurements between February 2022 (MoHo v3.2) and June/August 2023 (MoHo v4.0) for field operation (mean $\pm$ standard deviation) and bag/balloon experiments (mean $\pm$ maximum absolute error). MoHo v3.2 data taken form Büchau et al. (2023).

| | February 2022 | 2023 | |
		2nd of June	9th of August
Field Operation			
Duration	55 min.	Eight 30 sec. slices	22 min.
$\bar{\dot{V}} \pm \sigma(\bar{\dot{V}})$ [L s^{-1}]	2.90 ± 1.13	3.62 ± 0.45	3.32 ± 0.19
Bag/Balloon Experiments			
Experiments	1 & 7	1 - 9	1 - 5
$\bar{\dot{V}} \pm \Delta\bar{\dot{V}}_{\text{balloon, abs}}$ [L s^{-1}]	2.05 ± 0.9	2.80 ± 0.34	2.90 ± 0.17

Assuming both the measurements by Büchau in February 2022 and the most recent

measurements of June 2023 are representative for their respective season and an absence of any geogenic causes for mayor changes in the mofetta's flow rate, this indicates a possible seasonal dependency.

Based on observations by Büchau over the years, the height of the water table underneath which the mofetta is constantly submerged decreases during the summer. This is likely caused by a rise in evaporation combined with a decrease in precipitation. Such a shift in surface water abundance results in a drop in hydrostatic pressure that is exerted onto the upstreaming gas by the water column. Less force is needed to overcome this pressure, therefore less gas needs to built-up in order to surpass it and cyclic eruptions happen more frequently. This possible explanation is backed up by the requantification of the mofetta's cyclic eruptions, that concluded a rise in higher frequencies of the pressure waves created through its eruptions. This explanation is further supported by the measurements conduced by Mühlberger (2020) in 2020 who deployed the MoHo during the summer as well. Mühlberger measured an average volumetric flow rate of $3.99 \mathrm{~L\,s^{-1}}$ with the same cup anemometer design implemented by Büchau et al. (2023). Furthermore, measurements conducted for a mofettes system in the Czech Republic have quantified such a relationship between gas flux rates and hydrostatic pressure of the water table (Woith et al., 2022)

On a larger scale, this gives insight into a positive feedback system between climate and the natural CO_2 emissions of wet mofettes. May it be due to seasonal variability or anthropogenic climate change, droughts increase evaporation of surface water. In the context of wet mofettes, this increases their eruption frequency, or bubbling frequency depending on the scale of the mofetta, and therefore the flow of CO_2-rich gasses into the atmosphere. Due to CO_2's greenhouse gas nature, these gas masses contribute to the increase in global atmospheric temperature, making droughts more frequent and higher in intensity, creating a positive feedback loop (National Academies of Sciences et al., 2016).

In principle, this relationship is similar to the positive feedback carbon cycle found in peatlands. Here, a water table drop due to droughts is linked to a release of dissolved organic carbon. This release is caused by the shift from anaerobic to aerobic conditions that leads to the decomposition of organic matter that is exposed to air (Ise et al., 2008).

6 Conclusion

Despite the short measurement time of the MoHo v4.0 on the 9th of August 2023, individual sensor measurement and communication were implemented successfully. The calibration experiments allowed for the derivation of a flow rate formula that is highly adjusted to the mofetta's pressure conditions and MoHo's chimney design. Especially its ability to quantify negative flow rates of suction anomalies presents a considerable improvement to the cup anemometer which doesn't measure flow direction. High-resolution pressure data allows for the observation of quick changes in flow rate that may have been undetected before due to the cup anemometers inertia. Data transmission issues like the one experience on the 9th of August 2023 are probably software related and can likely be fixed through problem-solving via the trial and error method. The chimney's high modularity presents a considerable improvement in quick and easy field maintenance (e.g. troubleshooting, swapping modules, adding sensors) compared to the previous design. As in the prior MoHo version, the thermistor turned out to be a valuable asset to the measurement system for detecting and validating flow rate anomalies. Even though MoHo 4.0 is not ready for final field deployment yet, it lays the groundwork for a capable long-term monitoring device. The potential that long-term data presents in uncovering the dynamics of wet mofettes became evident through the flow rate and eruption frequency requantification and their comparison to previous measurements. The biggest challenge remains in finding a viable zero offset correction method that is not based on pre-determined correction values but instead re-calibrates itself automatically based on a robust metric or complementing measurement technique.

7 Outlook

A reoccurring situation where the differential pressure values captured within a balloon experiment are too small for the optimization to deliver a representative flow rate formula should be avoided. Through manually altering the balloon volume while a calibration experiment is taken, varying degrees of differential pressure values may be achievable.

A reliable and self-sufficient method for the zero offset correction needs to be implemented for the differential pressure flowmeter in order for it to deliver accurate results over long periods of time. One approach would be to reintroduce the cup anemometer from the MoHo v3.2 in the form of a new segment. Due to the cup anemometer's mechanical nature, it is not susceptible to a zero offset under no flow conditions. Therefore, it can be used to validate times of zero flow condition for which a new correction value for the pressure signal correction is determined and applied automatically. After the implementation of such an autarkic re-calibration method, useful values for the integrated volumetric flow rate and integrated CO_2 mass flux can be calculated by the microcontroller.

Due to the pressure dependency of the differential pressure flowmeter, it is influenced by the density and composition of the emitted gas. While the gas composition may not change significantly over time, the temperature variability needs to be accounted for. One option would be to repeatedly take balloon experiments across the year to collect a family of flow rate functions out of which a temperature dependency of the power law parameters may be derivable. By replacing the Bosch BMP384 with a more accurate micro-electromechanical system pressure sensor such as the Bosch BMP585, the temperature drift and signal noise of the differential pressure can be minimized (Bosch Sensortec GmbH, 2023). Furthermore, the sensor's temperature dependency should be quantified in a climate chamber experiment similar to the methods used by Büchau et al. (2023).

The possible climate dependent change in eruption frequency and volumetric flow rate that characterizes the mofetta needs to be further investigated and validated. For example, through the implementation of a water level measurement system, the relationship between water table height and flow rate can be quantified. Furthermore, to rule out that the difference in flow rate between winter and summer measurements is not due to too short measurement times and high variability of the mofetta's exhaust, long-term data must be collected.

8 Bibliography

Bosch Sensortec GmbH (May 2023). *BMP585 Barometric Pressure Sensor (v1.0)*. URL: https://www.bosch-sensortec.com/media/boschsensortec/downloads/datasheets/bst-bmp585-ds003.pdf (visited on 08/21/2023).

Büchau, Y. (2023a). *Data Analysis Tools for the CO_2 Project*. URL: https://gitlab.com/tue-umphy/co2mofetten/software/co2project (visited on 08/25/2023).

– (2023b). *sdfCAD*. URL: https://gitlab.com/nobodyinperson/sdf (visited on 08/24/2023).

Büchau, Y. G., C. Leven & J. Bange (2023). *A Portable low-cost Device to Quantify Advective Gas Fluxes from Mofettes into the Lower Atmosphere: First Application to Starzach Mofettes (Germany)*. EarthArXiv preprint of manuscsript submitted to Springer Environmental Monitoring and Assessment on 28.06.2023, revised on 10.10.2023 after one round of peer review, awaiting formal acceptance. DOI: 10.31223/X5ZX0D.

Gardner, E., J. Gardner & F. Udrea (Jan. 2023). "Micromachined Thermal Gas Sensors—A Review". In: *Sensors* 23, p. 681. DOI: 10.3390/s23020681.

LGRB (2023). *Landeserdbebendienst - Aktuelle Erdbeben*. URL: https://erdbeben.led-bw.de/ (visited on 08/24/2023).

OpenStreetMap contributors (2023). *Planet dump retrieved from https://planet.osm.org*. https://www.openstreetmap.org.

The SciPy community (2023). *scipy.optimize.minimize*. URL: https://docs.scipy.org/doc/scipy/reference/generated/scipy.optimize.minimize.html (visited on 08/25/2023).

Büchau, Y. G., B. van Kesteren, A. Platis & J. Bange (Oct. 2022). "An Autarkic Wireless Sensor Network to Monitor Atmospheric CO2 Concentrations". In: *Meteorologische Zeitschrift* 31.4, pp. 331–345. DOI: 10.1127/metz/2022/1125. URL: http://dx.doi.org/10.1127/metz/2022/1125.

Dörner, L. (2022). *Improving a device quantifying the natural CO_2 emissions of a mofetta*. Bachelor Thesis. University of Tübingen.

Fogleman, M. (2022). *sdf*. URL: https://github.com/fogleman/sdf (visited on 08/24/2023).

NumPy Developers (2022). *numpy.trapz*. URL: https://numpy.org/doc/stable/reference/generated/numpy.trapz.html (visited on 08/28/2023).

Woith, H., J. Vlček, T. Vylita, T. Dahm, T. Fischer, K. Daskalopoulou, M. Zimmer, S. Niedermann, J. A. Stammeier, V. Turjaková & M. Lanzendörfer (2022). "Effect of Pressure Perturbations on CO_2 Degassing in a Mofette System: The Case of Hartoušov, Czech Republic". In: *Geosciences* 13.1, p. 2. ISSN: 2076-3263. DOI: 10.3390/geosciences13010002. URL: http://dx.doi.org/10.3390/geosciences13010002.

Foken, T. (2021). *Springer Handbook of Atmospheric Measurements*. Springer Handbooks. Springer International Publishing. ISBN: 9783030521714. DOI: 10.1007/978-3-030-52171-4.

Bosch Sensortec GmbH (Nov. 2020). *BMP384 Digital pressure sensor (v1.0)*. URL: https://www.bosch-sensortec.com/media/boschsensortec/downloads/datasheets/bst-bmp384-ds003.pdf (visited on 08/03/2023).

Mühlberger, V. (2020). *Development of a Device Quantifying the Natural CO_2 Emissions of a Mofetta*. Bachelor Thesis. University of Tübingen.

Sensirion AG (Dec. 2020a). *Datasheet SHTC3 (v4)*. URL: https://www.sensirion.com/media/documents/643F9C8E/63A5A436/Datasheet_SHTC3.pdf (visited on 08/04/2023).

– (Oct. 2020b). *Datasheet STC31 (v1.1)*. URL: https://sensirion.com/media/documents/7B1D0EA7/61652CD0/Sensirion_Thermal_Conductivity_Datasheet_STC31_D1_1.pdf (visited on 08/07/2023).

Camarda, M., S. De Gregorio, G. Capasso, R. M. Di Martino, S. Gurrieri & V. Prano (2019). "The monitoring of natural soil CO2 emissions: Issues and perspectives". In: *Earth-Science Reviews* 198, p. 102928. ISSN: 0012-8252. DOI: https://doi.org/10.1016/j.earscirev.2019.102928. URL: https://www.sciencedirect.com/science/article/pii/S0012825219301151.

Hörmle, K. (2019). *CO_2-Emission Estimation of a Mofette with a Low-Cost Approach*. Master Thesis. University of Tübingen.

Lübben, A. & C. Leven (2018). "The Starzach site in Southern Germany: a site with naturally occurring CO2 emissions recovering from century-long gas mining as a natural analog for a leaking CCS reservoir". In: *Environmental Earth Sciences* 77 (8), p. 316. DOI: https://doi.org/10.1007/s12665-018-7499-y. URL: https://doi.org/10.1007/s12665-018-7499-y.

Tran, A. V., X. Zhang & B. Zhu (2018). "Mechanical Structural Design of a Piezoresistive Pressure Sensor for Low-Pressure Measurement: A Computational Analysis by Increases in the Sensor Sensitivity". In: *Sensors* 18.7. ISSN: 1424-8220. DOI: 10.3390/s18072023. URL: https://www.mdpi.com/1424-8220/18/7/2023.

Fischer, T., C. Matyska & J. Heinicke (2017). "Earthquake-enhanced permeability – evidence from carbon dioxide release following the M_L 3.5 earthquake in West Bohemia". In: *Earth and Planetary Science Letters* 460, pp. 60–67. ISSN: 0012-821X. DOI: https://doi.org/10.1016/j.epsl.2016.12.001. URL: https://www.sciencedirect.com/science/article/pii/S0012821X16307014.

Sarzhanov, D., V. Vasenev, I. Vasenev, Y. Sotnikova, O. Ryzhkov & T. Morin (2017). "Carbon stocks and CO_2 emissions of urban and natural soils in Central Chernozemic region of Russia". In: *CATENA* 158, pp. 131–140. ISSN: 0341-8162. DOI: https://doi.org/10.1016/j.catena.2017.06.021. URL: https://www.sciencedirect.com/science/article/pii/S0341816217302205.

Anderson, T. R., E. Hawkins & P. D. Jones (2016). "CO_2, the greenhouse effect and global warming: from the pioneering work of Arrhenius and Callendar to today's Earth System Models". In: *Endeavour* 40.3, pp. 178–187. ISSN: 0160-9327. DOI: https://doi.org/10.1016/j.endeavour.2016.07.002. URL: https://www.sciencedirect.com/science/article/pii/S0160932716300308.

Cook, J., N. Oreskes, P. T. Doran, W. R. L. Anderegg, B. Verheggen, E. W. Maibach, J. S. Carlton, S. Lewandowsky, A. G. Skuce, S. A. Green, D. Nuccitelli, P. Jacobs, M. Richardson, B. Winkler, R. Painting & K. Rice (Apr. 2016). "Consensus on consensus: a synthesis of consensus estimates on human-caused global warming". In: *Environmental Research Letters* 11.4, p. 048002. DOI: 10.1088/1748-9326/11/4/048002. URL: https://dx.doi.org/10.1088/1748-9326/11/4/048002.

National Academies of Sciences, E., D. Studies, B. Climate & C. Attribution (2016). *Attribution of Extreme Weather Events in the Context of Climate Change*. National Academies Press. ISBN: 9780309380973. URL: https://books.google.de/books?id=WWEpDQAAQBAJ.

Schütze, C., K. Bräuer, P. Dietrich, V. Engnath, M. Gisi, G. Horak, C. Leven, A. Lübben, I. Möller, M. Nierychlo, S. Schlömer, A. Schuck, U. Serfling, A. Simon, T. Streil & U. Sauer (2015). "MONACO—Monitoring Approach for Geological CO2 Storage Sites Using a Hierarchical Observation Concept". In: *Geological Storage of CO2 – Long Term Security Aspects: GEOTECHNOLOGIEN Science Report No. 22*. Ed. by A. Liebscher & U. Münch. Cham: Springer International Publishing, pp. 33–57. ISBN: 978-3-319-13930-2. DOI: 10.1007/978-3-319-13930-2_2. URL: https://doi.org/10.1007/978-3-319-13930-2_2.

Farahani, H., R. Wagiran & M. N. Hamidon (2014). "Humidity Sensors Principle, Mechanism, and Fabrication Technologies: A Comprehensive Review". In: *Sensors* 14.5, pp. 7881–7939. ISSN: 1424-8220. DOI: 10.3390/s140507881. URL: https://www.mdpi.com/1424-8220/14/5/7881.

Langeheinecke, K., P. Jany, G. Thieleke, K. Langeheinecke & A. Kaufmann (Nov. 2013). *Thermodynamik für Ingenieure*. 9th ed. Springer Vieweg Wiesbaden. ISBN: 978-3-658-03169-5. DOI: 10.1007/978-3-658-03169-5.

Bird, J. (2010). *Electrical and Electronic Principles and Technology*. 2nd ed. Newnes, p. 57. ISBN: 0 7506 5778 2.

Ise, T., A. L. Dunn, S. C. Wofsy & P. R. Moorcroft (2008). "High sensitivity of peat decomposition to climate change through water-table feedback". In: DOI: https://doi.org/10.1038/ngeo331.

Atkins, P. & J. de Paula (2006). *Atkins' physical chemistry*. 8th ed. W. H. Freeman and Company. ISBN: 0-7167-8759-8.

Bentley, J. P. (2005). *Principles of measurement systems*. 4th ed. England: Pearson Education. ISBN: 0-13-043028-5.

Wang, G. (2005). *CMOS Bandgap References and Temperature Sensors and Their Applications*. Optima Grafische Communicatie, p. 1. ISBN: 90-9018727-8. URL: http://resolver.tudelft.nl/uuid:cc957424-7611-4dd5-b84c-91ee9b1283d0.

Fenghour, A., W. A. Wakeham & V. Vesovic (Jan. 1998). "The Viscosity of Carbon Dioxide". In: *Journal of Physical and Chemical Reference Data* 27.1, pp. 31–44. ISSN: 0047-2689. DOI: 10.1063/1.556013.

Marty, B. & I. N. Tolstikhin (1998). "CO_2 fluxes from mid-ocean ridges, arcs and plumes". In: *Chemical Geology* 145.3, pp. 233–248. ISSN: 0009-2541. DOI: https://doi.org/10.1016/S0009-2541(97)00145-9. URL: https://www.sciencedirect.com/science/article/pii/S0009254197001459.

Martini, M. (1997). "CO_2 emission in volcanic areas: case histories and hazards". In: *Plant Responses to Elevated CO_2: Evidence from Natural Springs*. Ed. by A. Raschi, F. Miglietta, R. Tognetti & P. v. Gardingen. Cambridge University Press, pp. 34–44. DOI: 10.1017/CBO9780511565236.005.

Stolz, J. (1978). *A Universal Equation for the Calculation of Discharge Coefficients of Orifice Plates*. URL: https://books.google.de/books?id=7HYCGwAACAAJ.

Nelder, J. A. & R. Mead (Jan. 1965). "A Simplex Method for Function Minimization". In: *The Computer Journal* 7.4, pp. 308–313. ISSN: 0010-4620. DOI: 10.1093/comjnl/7.4.308. eprint: https://academic.oup.com/comjnl/article-pdf/7/4/308/1013182/7-4-308.pdf. URL: https://doi.org/10.1093/comjnl/7.4.308.

Powell, M. J. D. (Jan. 1964). "An efficient method for finding the minimum of a function of several variables without calculating derivatives". In: *The Computer Journal* 7.2, pp. 155–162. ISSN: 0010-4620. DOI: 10.1093/comjnl/7.2.155. eprint: https://academic.oup.com/comjnl/article-pdf/7/2/155/959784/070155.pdf. URL: https://doi.org/10.1093/comjnl/7.2.155.